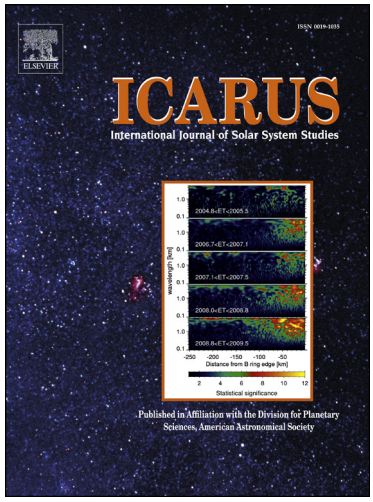

Atmospheric superrotation in an idealized GCM: Parameter dependence of the eddy response

João Rafael Dias Pinto, Jonathan Lloyd Mitchell

PII: S0019-1035(14)00228-0
DOI: http://dx.doi.org/10.1016/j.icarus.2014.04.036
Reference: YICAR 11066

To appear in: *Icarus*

Received Date: 29 October 2013
Revised Date: 17 April 2014
Accepted Date: 17 April 2014

Please cite this article as: Pinto, o.R.D., Mitchell, J.L., Atmospheric superrotation in an idealized GCM: Parameter dependence of the eddy response, *Icarus* (2014), doi: http://dx.doi.org/10.1016/j.icarus.2014.04.036

Atmospheric superrotation in an idealized GCM: parameter dependence of the eddy response

by

João Rafael Dias Pinto[1,2], Jonathan Lloyd Mitchell[2]

[1]Department of Atmospheric Sciences. Institute of Astronomy, Geophysics and Atmospheric Sciences, University of São Paulo. Rua do Matão, 1226, CEP 05508-090, Cidade Universitária, São Paulo, SP, Brazil. (joao.dias@iag.usp.br)

[2]Department of Earth, Planetary and Space Sciences, Department of Atmospheric and Oceanic Sciences. University of California, Los Angeles. 595 Charles Young Drive East, Box 951567, Los Angeles, CA, 90095, USA. (jonmitch@ucla.edu)

ABSTRACT

Idealized Earth-like general circulation models (GCMs) have been extensively used to study superrotation on so-called "slowly rotating" bodies like Venus and Titan, however they tend to have difficulty producing superrotation if only the rotation rate is reduced to Titan- or Venus-like values. The Rossby number, $Ro = U/2\Omega L$, which characterizes the influence of rotation on the circulation, is small for Earth but large for both Venus and Titan. However, the differences in other non-dimensional control parameters are often ignored in idealized planetary circulation studies. In this study we use a simplified Earth-like GCM to demonstrate the importance of the other non-dimensional parameters in obtaining a superrotating flow, and identify the wave-modes responsible for generating and maintaining superrotation. We show that superrotation only emerges on a planet of slow rotation rate if the atmospheric thermal inertia is simultaneously increased; alternatively, superrotation is obtained if the only planetary radius is reduced. When only the rotation rate is reduced, a nearly axisymmetric circulation with intense Hadley cells is produced that prevents strong and persistent winds over the equator. The mechanism for generating and maintaining superrotation in the model involves a coupling between equatorial and high-latitude waves. However, the generation involves equatorial Kelvin-like waves and maintenance involves equatorial Rossby-like waves.

Key words: Atmosphere, dynamics; Meteorology; Terrestrial planets; Titan, atmosphere; Venus, atmosphere.

1. Introduction

Nondimensional variables involving typical values of velocities, length, diffusivity, density, viscosity and rotation rate, play a key role in characterizing many dynamical aspects of a flow. Among them, the Rossby number (*R*o) is one of the most important parameters in geophysical fluid mechanics to characterize dynamical properties of the flow. Defined as

$$R_O = U/2\Omega L \quad (1)$$

where U, 2Ω and L are typical magnitudes of zonal wind, planetary rotation and flow length scales, it relates the ratio of advection to Coriolis force for a given flow of a rotating fluid or a large scale atmospheric motion (Holton, 2004; Vallis, 2006). The geostrophic approximation holds for small values of *R*o, as is the case for Earth's mid and high latitudes.

The terrestrial bodies in the solar system with substantial atmospheres, Earth, Mars Venus and Saturn's moon Titan, present two distinct regimes of atmospheric circulation. Figure 1 shows that at global scales, *R*o << 1 for Earth and Mars while *R*o > 1 for Venus and Titan. The mean zonal structures of these atmospheres roughly exhibit two different regimes, which we define as the classic and superrotating, and describe in more detail below.

Earth and Mars are fast rotating and large terrestrial bodies, which gives them rather small global values of *R*o ~ 0.01. In this regime, there are substantial differences between the circulation in low and high latitudes. At low latitudes, the meridional circulation is characterized by upward motion of relatively warm air at the equator and sinking of cold air at subtropical latitudes along the latitudinal plane, which develops prograde zonal flow, on the poleward edge of each tropical overturning circulation, or Hadley cell (Figure 1). At higher latitudes, on the other hand, the flow is dominated by large scale eddies which arise from baroclinic instability (Holton, 2004; Vallis, 2006). Seasonal cycles complicate this picture somewhat, and we will not consider their effects here.

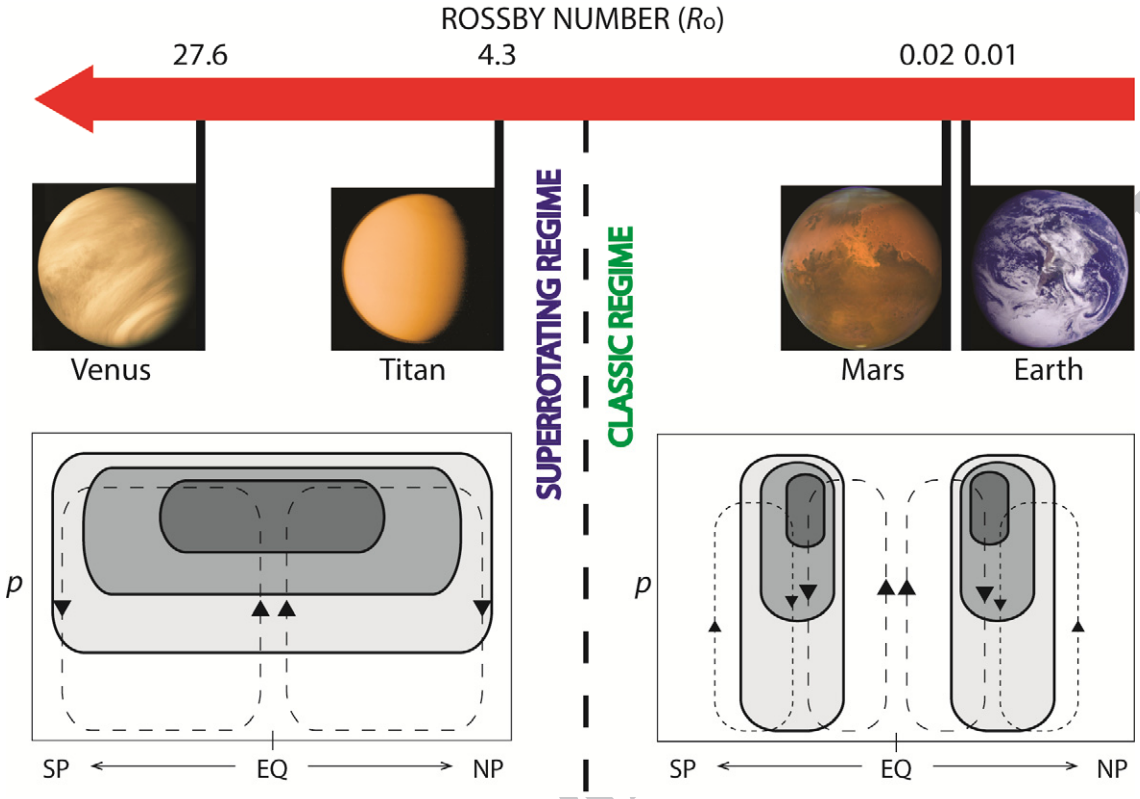

Figure 1. Schematic view of the different Rossby numbers (*R*o) and circulation regimes found on the terrestrial bodies of the solar system with substantial atmospheres. *R*o was computed based on typical scales of zonal winds (around 100 m s^{-1} for Venus and Titan and 10 m s^{-1} for Earth and Mars), rotation rate, and planetary radius. The lower panels depicts a hypothetical vertical cross section of zonal mean zonal wind (shaded, arbitrary scale) and mean overturning circulation (dashed lines, arbitrary scales) characteristic of each body's atmospheres. See text for more details. (Photo credits: NASA/JPL).

Since the rotation rates of Venus and Titan are slower compared to Earth and Mars' (the rotation period is about 16 days for Titan and around 240 days for Venus), numerical studies often focus on Earth-like atmospheres under slow rotation (Williams, 1988a,b, Navarra and Boccaletti, 2002; Walker and Schneider, 2006 Williams, 1988a; Del Genio and Suozzo, 1987; Del Genio et al., 1993; Williams, 2003). In parallel, simulations using numerical models set for either simplified or fully parameterized physical process (as for example, turbulent dissipation at the boundary layer, radiative transfer, chemical reactions and aerosols) of Venus (Yamamoto and Takahashi, 2003; Lee et al., 2005; Lee et al., 2007; Hollingsworth et al., 2007; Lebonnois et al., 2010 and Parish et al., 2011) and Titan (Hourdin et al., 1995; Tokano et al., 1999; Tokano, 2007; Richardson et al., 2007; Friedson et al., 2008;

Newman et al, 2011; Mitchell et al. 2011, 2012) have been performed in order to gain a more complete and accurate view of the general circulation patterns (and their time dependence) for each body. A common feature of all these studies is that the Hadley cell is larger in meridional extent (Figure 1) and poleward heat fluxes efficiently act to reduce the latitudinal contrast of the temperature. Since the Rossby deformation radius is proportional to Ω^{-1} (Eady, 1949; Vallis, 2006), baroclinic instability weakens in this regime of higher Rossby numbers due to the fact that the typical unstable wavelength no longer fits on of the planet (Williams, 1988a,b; Navarra and Boccaletti, 2002). Due to the large obliquity of Titan (around 26.7° to the ecliptic) the Hadley cell is also expected to have strong seasonal variation changing from a situation depicted on Figure 1, with a symmetric pair of overturning circulation at the equator during the equinox, to a single inter-hemispheric Hadley cell. Structural changes regarding to the mean overturning circulation from an Earth to a higher *R*o regime are common to the modeling studies.

However, few models today are able to reproduce the full strength of the zonal wind distribution on Venus and Titan. Both in situ and indirect observation from each body (for example Bougher et al. 1997; Kostiuk et al., 2001; Bird et al., 2005 and Widemann et al., 2008) have shown strong zonal flow with magnitude of 100 m s^{-1} being the dominant component of the atmospheric circulation even at the equator. Such strong zonal winds at the upper level of Venus and Titan's equatorial atmospheres are in, so-called, superrotation. Some models produce only weak superrotation with zonal wind s of 2 – 40 m s^{-1} at the equator (e.g., Tokano et al., 1999; Lee et al., 2007; Richardson et al., 2007; Friedson et al., 2008; and Lebonnois et al., 2010) while others produce stronger equatorial winds (Hourdin et al., 1995; Yamamoto and Takahashi, 2003; and Newman et al., 2011) more in-line with observations (Widemann et al., 2008; Kostiuk et al., 2001, for example). This discrepancy

among similar models has yet to be understood, making the study of superrotating flow a challenging subject in geophysical fluid dynamics.

Through eq. 1, a larger *R*o (for the same wind typical scale *U*) could be achieved by either slowing the rotation rate of the planet down or decreasing the typical horizontal length scale on which the winds occur. When Earth-like models are run at slower rotation rates, they tend to produce strong jets at higher latitudes but also tend to fail in reproducing superrotating flow over the equator (see for example in Williams 1988a; Navarra and Boccalleti, 2002). Mitchell and Vallis (2010) changed the Rossby number by decreasing the planetary radius in an idealized Earth-like model, and showed that in the cases with Ro > 1, the dynamics adjusted itself in such way that superrotation was produced. Therefore different outcomes can be obtained in simplified models when either the rotation rate or the planetary radius is reduced. This study aims to identify how these differences are obtained in a simplified Earth-like GCM by describing the momentum balance achieved when changing rotation rate versus planetary radius. A key goal is to identify the wave modes that maintain the superrotation at the equator in the steady state. The study is organized as follows: section 2 describes the theoretical framework and the numerical experiments, the section 3 presents the momentum budgets and eddy diagnostics of our experiments and we conclude in section 4.

2. Methodology

2.1. Dimensionless governing equations and control parameters

In our simplified modeling framework, the three-dimensional flow is described by the horizontal momentum and thermodynamics equations in which the diabatic and frictional effects are given by a linear Rayleigh friction and Newtonian cooling

$$\frac{\partial \vec{u}}{\partial t} + (\vec{V} \cdot \nabla)\vec{u} + \vec{f} \times \vec{u} = -\nabla\Phi - \frac{\vec{u}}{\tau_f} \tag{2}$$

$$\frac{\partial \theta}{\partial t} + (\vec{V} \cdot \nabla)\theta = -\frac{(\theta - \theta_{eq})}{\tau_\alpha} \tag{3}$$

where, $\vec{u} = u\vec{i} + v\vec{j}$ and $\vec{V} = u\vec{i} + v\vec{j} + \omega\vec{k}$ are the two-dimensional and three-dimensional wind fields in pressure vertical coordinates and ω is the vertical pressure velocity in this coordinate; $f = 2\Omega sin\phi$ is the Coriolis parameter; Φ is the geopotential, and τ_f and τ_α are the characteristic frictional and thermal damping time scales of the simplified parameterizations. By traditional scaling arguments, these equations can be written in terms of nondimensional variables and parameters, indicated by the "hats" (see sections 2.12.1 and 5.1 of Vallis, 2006) as:

$$\frac{\partial \hat{\vec{u}}}{\partial \hat{t}} + R_O\left(\hat{\vec{V}} \cdot \nabla\right)\hat{\vec{u}} + \hat{\vec{f}} \times \hat{\vec{u}} = -\nabla\hat{\Phi} - E_K\hat{\vec{u}} \tag{4}$$

$$\frac{\partial \hat{\theta}}{\partial \hat{t}} + R_O\left(\hat{\vec{V}} \cdot \nabla\right)\hat{\theta} = -\frac{(\hat{\theta} - \hat{\theta}_{eq})}{\hat{\tau}_\alpha} \tag{5}$$

In eqs. 4 and 5, $R_O = U/2\Omega L$ represents the Rossby number, $E_K = 1/2\Omega\tau_f$ the Ekman number and $\hat{\tau}_\alpha = 2\Omega\tau_\alpha$ a thermal damping number. These three nondimensional parameters describe both dynamical and thermal properties of the flow, and therefore govern the behavior of the system once the obtained circulation can be seen as a combination of

values of these different nondimensional parameters. For instance, the Ekman number governs the magnitude of friction in the boundary layer whereas the thermal number governs the thermal inertia of the atmosphere.

2.2. Numerical experiments

The numerical simulations were performed with version 3.3.1 of the Weather Researcher and Forecast Model (WRF; Skamarock et al., 2008). Although originally designed for a regional domain, this model has been used for global simulations in Mars and Titan atmospheres (Richardson et al., 2007; Newman et al., 2011 and Toigo et al., 2012). The global version assumes the Euler equations in flux form on a rotating spherical surface for an ideal gas in hydrostatic equilibrium. In order to isolate the main dynamical mechanism present in the superrotating state, all physical parameterizations related to short- and long-wave radiation, turbulence, surface fluxes and convection are substituted by a simple forcing and dissipation. This is a severe simplification, but the resulting circulation regime is thought to be free of the complication of these physical processes and thus cleanly reveal the characteristics of the dynamics. Here we used the Held-Suarez benchmark (Held and Suarez, 1994; hereafter HS94) in which the Newtonian cooling and Rayleigh friction are prescribed mathematically by,

$$\left(\frac{d\theta}{dt}\right)_{Diab} = -k_a(\phi,p)\left[\theta - \theta_{eq}(\phi,p)\right] \tag{6}$$

$$\left(\frac{d\vec{u}}{dt}\right)_{Fric} = -k_f(p)\vec{u} \tag{7}$$

where,

$$\theta_{eq}(\phi,p) = max\left\{200\ K, \left[315\ K - (\Delta T)_y \sin^2\phi - (\Delta\theta)_z \ln\left(\frac{p}{p_0}\right)\cos^2\phi\right]\left(\frac{p}{p_0}\right)^{\kappa}\right\}$$

(8)

$$k_a(\phi, p) = \frac{1}{\tau_a}\left[1 + 9\,max\left(0, \frac{\sigma - \sigma_b}{1 - \sigma_b}\right)\cos^4\phi\right] \quad (9)$$

$$k_f(p) = \frac{1}{\tau_f}\,max\left(0, \frac{\sigma - \sigma_b}{1 - \sigma_b}\right) \quad (10)$$

Here $\sigma = p/p_0$ is the pressure-normalized sigma-level and, k_a, k_f and θ_{eq} are respectively, the pressure, the thermal and dissipation coefficients and the forcing potential temperature equilibrium profile. The dimensional constants are, $(\Delta T)_y$ the horizontal temperature contrasts, $(\Delta\theta)_z$ the vertical temperature contrast, p_0 the surface pressure, and σ_b is the sigma-level of the boundary layer, which are held fixed constant in all our experiments. The latitudinal cross-sections of forcing temperature profile and the thermal and frictional time scales as well as the parameter values used in the simulations are depicted in Figure 2.

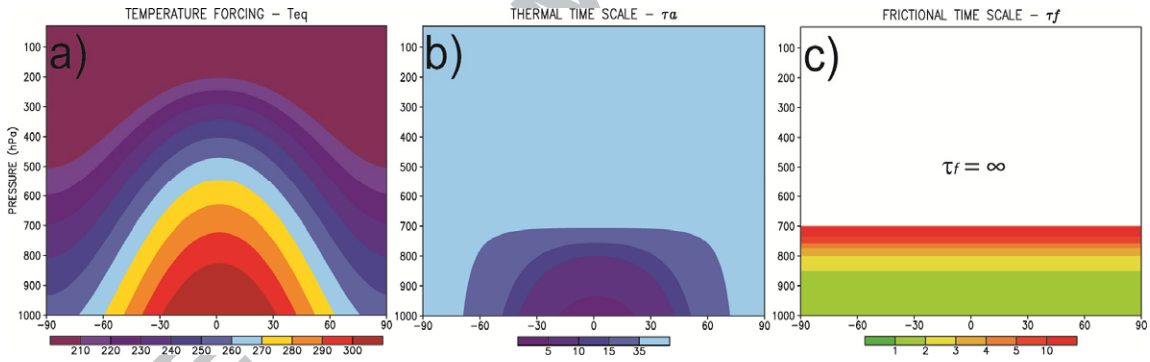

Figure 2. Vertical cross section of the equilibrium temperature and the characteristic thermal and frictional time scales used in the Held-Suarez benchmark, which we use to force our model experiment. The values used for the constants in eqs. (6) - (10) are $(\Delta T)_y = 60K$, $(\Delta\theta)_z = 10K$, $p_0 = 1000\ hPa$, $\sigma_b = 0.7$, $\kappa = R/c_p = 2/7$, $\tau_a = 40\ days$ and $\tau_f = 1\ day$.

The temperature forcing (eq. 8) is intended to approximate an equilibrium profile of a zonally symmetric atmosphere in which only radiation and convection affect the thermal distribution (i.e. without dynamics). Temperatures decrease monotonically through the troposphere and the stratosphere is treated as an isothermal layer. Since there is no exchange between the atmosphere and the underlying surface, the Newtonian relaxation towards this forcing profile (eq. 6) has the effect of near-surface adiabatic heating, radiative cooling and

convection in the free troposphere through spatial dependence of the thermal relaxation time (eq. 9, Figure 2). This relaxation time is 40 days above $\sigma_b = 0.7$ and becomes smaller toward the surface and the tropical region. Rayleigh friction representing dissipation in the boundary layer (eqs. 7 and 10) is applied below $\sigma_h = 0.7$. The frictional time scales (Figure 2) ranges with height from 1 day at the near surface to infinity in the free atmosphere (which means that the friction has no role in this layer). No friction is applied above the level $\sigma_b = 0.7$ aside from a small artificial attenuation given by the 2D Smagorinsky first order closure (with the empirical constant c_s set 0.25, Smagorinsky, 1963) scheme and second order diffusion terms in order to avoid numerical instabilities. According to Skamarock et al. (2008), WRF uses polar filtering in order to reduce the timestep restriction associated with the convergence of the gridlines toward the poles. For a given variable, this filtering is accomplished by applying a one-dimensional Fourier transform to this variable over a constant latitude circle and poleward a specified latitude value (here defined as the default value of 45°). The Fourier coefficients with wavenumbers above a prescribed threshold are truncated, after which a transformation back to physical space is applied, completing the filter step (Skamarock et al., 2008).

With the goal of understanding the influence of increasing the Rossby number, we devised a set of numerical experiments intended to highlight its importance relative to the other non-dimensional numbers by either decreasing the rotation rate or the planetary radius. With a characteristic length scale given by the planetary radius a the local Rossby number is defined as

$$R_o = \frac{U}{2\Omega \sin\phi \; a\cos\phi} \tag{11}$$

We run two sets of numerical experiments: in the first one named a^* (= a/a_{earth}), the radius is varied from Earth's to values 20 times smaller, which roughly corresponds to the

radius of 280 km used in the superrotating experiment by Mitchell and Vallis (2010). In the second experiment, referred to Ω^* (= Ω/Ω_{Earth}), we reduced the rotation rate by the same factor, from Earth's values to values 20 times smaller. The values of the constants and nondimensional numbers for the whole set of numerical experiments are given in Table 1.

The simulations are initialized from an isothermal and motionless atmosphere and run with 32 vertical levels and 3.0° x 3.0° horizontal grid spacing. In order to integrate the model for equivalent dynamical/inertial times, the numerical experiments are run for 10 years, or 3,650 days for simulations with Earth's rotation rate and 73,000 days for those with Ω^* = 1/20. The data output are given at each 3 files per day. Unless otherwise stated, the results presented here are averaged over the last year of each experiment at the statistically steady phase. Figure 3 shows the total kinetic energy at the equilibrium for all experiments during this final year of the simulations.

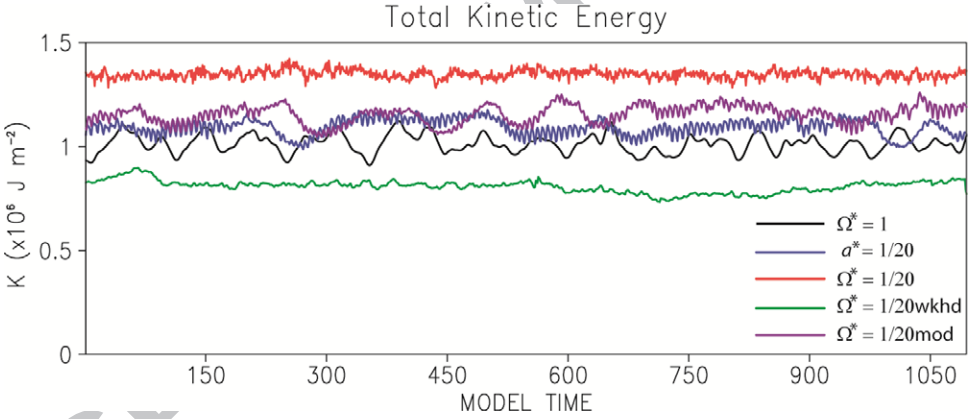

Figure 3. Vertically-integrated total kinetic energy (x10^6 J m^{-2}) during the last year of the simulations for each experiment. Apart from small oscillations the kinetic energy is constant, indicationg a steady state has been achieved.

3. Results

3.1. Circulation regimes at low and high Rossby numbers

Figure 4 depicts the vertical cross section of time- and zonal-mean zonal winds, temperature and overturning mass flux, which is expressed by a stream function

$\psi = 2\pi a \cos\phi \int_{p_s}^{p} [\bar{v}]\, dp/g$. In the Earth-like regime (Figure 4a and 4b) the model reproduces the main features of the general circulation, being dominated by two westerly (prograde) subtropical jets in mid-latidudes (peak of 30 m s^{-1} centered about 40° at 200 hPa), and the weaker near-surface easterlies in the equatorial region. The baroclinic thermal structure given by the temperature gradients at mid- and high-latitudes is also reproduced, as well as the overturning circulation of the Hadley cells in the tropics and the Ferrell cells at high latitudes. The Hadley cell is a two-dimensional, axisymmetric overturning. In reality, there can be zonal asymmetric circulation created by land-sea distribution (Walker cell) and topography. However since these two forcing features are absent in the model configuration, the overturning circulation can be purely expressed by the axisymmetric structure given by Figure 4b.

In the $\Omega^* = 1/20$ experiment, the circulation is in a higher *R*o regime, and the subtropical jets shift to high latitudes and become stronger (Figure 4c). The Hadley cell is both wider in latitude and stronger (with peak of 500×10^9 kg s^{-1}), which in turn decreases the temperature contrasts in its range of influence, as can be observed in Figure 4d. The latitudinal expansion of the Hadley cell shifts the subtropical jets and baroclinic zones poleward, thus promoting high-latitude jet formation. These features have been noted by other studies of circulation under slow rotation rates (Hunt, 1979; Williams and Holloway, 1982, Williams, 1988a,b; Navarra and Boccaletti, 2002; Walker and Schineider, 2006). A general conclusion is the latitudinal extension of the mean meridional circulation increases with smaller rotation rate, transporting heat further poleward and decreasing the latitudinal thermal gradients over much of the globe. However, a significant baroclinic zone remains poleward of 60º N/S latitudes. The poleward shift of the jets may be partly understood from an axisymmetric and nearly inviscid perspective, in which the latitude of a jet maximum should increase as the Rossby number increases (Held and Hou, 1980, Mitchell and Vallis, 2010). In

this experiment, the tropospheric zonal circulation is dominated by two, strong jets, and there is no occurrence of westerly, superrotating winds at the equator. In the narrow baroclinic zone around the latitudes of 80º - 90º N/S, a weaker Ferrell cell (two orders of magnitude weaker than the Hadley cell) is observed in each hemisphere (Figure 4d).

However, another pattern of winds emerges when the planetary radius is reduced in experiment a^* = 1/20. The flow is predominantly prograde (westerly) in much of the atmosphere, except at the lower levels and latitudes where they are easterly (Figure 4e and 4f). A single jet is located in the equatorial region (around 25-30 ms^{-1}), which is characteristic of a strongly superrotating state. The latitudinal extension of the mean meridional circulation (about 60° of width) did not vary considerably between the two experiments, whereas its strength is more than three orders of magnitude less (peak of $1.2x10^9$ kg s^{-1}) than the Ω^* = 1/20 experiment. In the higher latitudes a weak Ferrell cell is observed even though the mean thermal state has a more barotropic configuration. Apart from small differences in intensity, the superrotating zonal wind pattern in this configuration is in agreement with the experiments described in Mitchell and Vallis (2010) in which the transition to the superrotation was observed for thermal Rossby number bigger than 1.0 (see their Ro_T = 10.5 simulation).

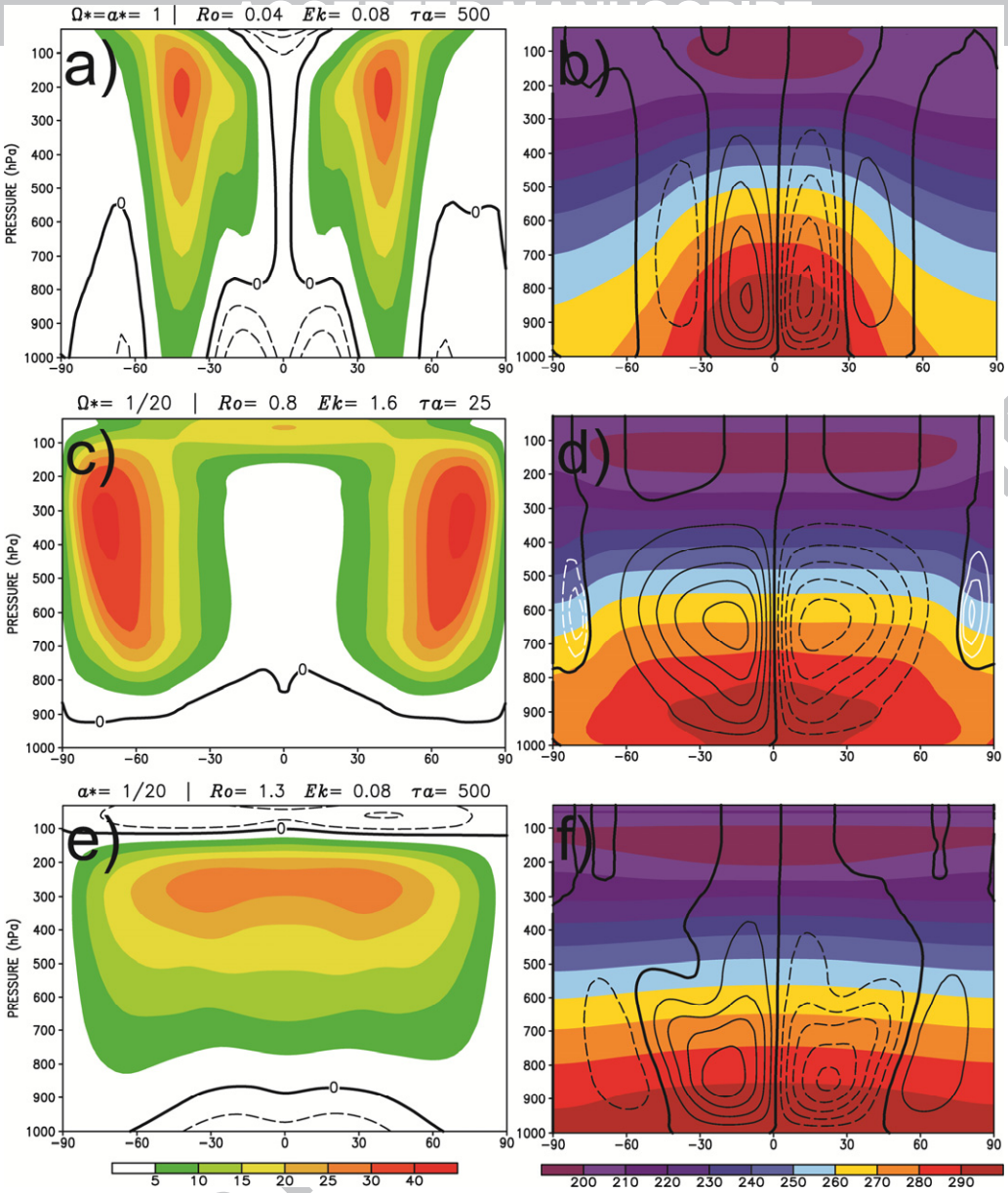

Figure 4. Vertical cross-sections of the time- and zonal-mean variables. The left panels are the zonal wind component (westerly winds in shaded; easterlies in dashed line with contour each 3 m s^{-1}). The right panels are temperature (shaded, K) and stream function ψ (contour, kg s^{-1}). a) and b) Experiment control, Earth-like case (ψ contours each $20x10^9$ kg s^{-1}); c) and d) Experiment Ω*= 1/20 (ψ black contours each $100x10^9$ kg s^{-1}, white contours each $3x10^9$ kg s^{-1}); e) and f) Experiment a*= 1/20 (ψ contours each $0.3x10^9$ kg s^{-1}). The nondimensional parameters were computed based on the values in Table 1 and Figure 5 (see text for more details).

Genio et al. (1993) and others noticed that many Earth-based models fail to produce superrotation if run in a slower rotation configuration, but they follow the general behavior (barotropic thermal structure, wider Hadley cells) as described above. Since in our two simulations, one succeeded and one failed to produce a superrotating zonal jet at the equator, it is important to analyze how the winds at the equator are maintained in a time- and zonal-

mean framework. In the following section, we diagnose the components of the circulation (mean meridional circulation and transient eddies) that are responsible for convergence and divergence of momentum at the equator in both non-superrotating and superrotating states.

3.2. Mean convergence of momentum and net accelerations in the steady state

The time- and zonal-mean zonal momentum equation written in a flux form is given by:

$$\frac{\partial[\bar{u}]}{\partial t} + \frac{1}{a\cos\phi}\frac{\partial}{\partial\phi}(\cos\phi\,[\overline{uv}]) + \frac{\partial}{\partial p}[\overline{u\omega}] - 2\Omega\sin\phi\,[\bar{v}] + \frac{2\Omega\cos\phi\,[\bar{\omega}]}{\rho g} - \frac{\tan\phi}{a}[\overline{uv}] + \frac{[\overline{u\omega}]}{a\rho g} = [\bar{F}_x] \quad (12)$$

where u, v and ω are the wind components, ϕ is the latitude, a the planetary radius, p pressure and F_x the frictional processes. According to Lorenz (1967) the transport of momentum in the atmosphere can be decomposed in three components related to the mean meridional circulation, transient and stationary eddies. Based the notation on Peixoto and Oort (1992), both meridional and vertical momentum fluxes can be written as a sum of these components:

$$[\overline{uv}] = [\bar{u}][\bar{v}] + [\overline{u'v'}] + [u^*v^*]$$
$$[\overline{u\omega}] = [\bar{u}][\bar{\omega}] + [\overline{u'\omega'}] + [u^*\omega^*] \quad (13)$$

where bar denotes average in time, brackets the zonal mean; their departures are given by, respectively by the prime and stared terms . Since stationary forcings are absent in the model (i.e., the HS94 benchmark is axisymmetric) stared terms are absent. Since $\frac{[\overline{uw}]}{a\rho g}$ and $\frac{2\Omega\cos\phi[\bar{w}]}{\rho g}$ terms are too small compared to the others, eq. 12 can be written as:

$$\frac{\partial[\bar{u}]}{\partial t} = -\frac{1}{a\cos\phi}\frac{\partial}{\partial\phi}(\cos\phi\,[\bar{u}][\bar{v}]) + 2\Omega\sin\phi\,[\bar{v}] - \frac{\partial}{\partial p}[\bar{u}][\bar{\omega}] + \frac{\tan\phi}{a}[\bar{u}][\bar{v}] - \frac{1}{a\cos\phi}\frac{\partial}{\partial\phi}(\cos\phi\,[\overline{u'v'}]) + \frac{\tan\phi}{a}[\overline{u'v'}] - \frac{\partial}{\partial p}[\overline{u'\omega'}] + [\bar{F}_x] \quad (14)$$

Eq. 14 establishes that the net acceleration (deceleration) of the time- and zonal-mean zonal winds are due to the combination of the convergence (divergence) of the momentum transport by the mean meridional cells and transient eddies, the Coriolis and the metric terms. The momentum balance postulated in the Gierasch-Rossow-Williams mechanism, as an attempt to understand how superrotation is maintained (GRW, Gierasch, 1975; Rossow and Williams, 1979), involves the transport by the overturning circulation ($[\bar{u}][\bar{v}]$ and $[\bar{u}][\bar{\omega}]$), and that of non-axisymmetric disturbances ($[\overline{u'v'}]$ and $[\overline{u'\omega'}]$) generated by the instabilities of a barotropically unstable high latitude jet (Rossow and Williams, 1979; Hourdin et al., 1995; Williams, 2003; Luz and Hourdin, 2003). For the present analysis, the terms related to the cell transports (including the coriolis and metric terms) are summed together to account for the combined effects of the overturning circulations.

Figure 5 depicts the mass-weighted vertical integral of net acceleration/deceleration of the zonal wind. The combined effects of the cells and transient eddies are divided in two vertical layers: 1000 – 600 hPa where the effects of the frictional boundary layer of the model are important, and 600 – 100 hPa for the free troposphere. All terms are weighted by the atmospheric mass of the vertical layer, $A^{p}_{p0} = \int_{p0}^{p} A dp / \int_{p0}^{p} dp$, with a generic variable A, and bottom and top level pressures p_0 and p. Since the magnitudes of the accelerations in mid- and high-latitudes and near the equator are different, they are displayed separately on different scales. For reasons of symmetry only the higher latitudes (above 45° S) of the Southern Hemisphere are shown.

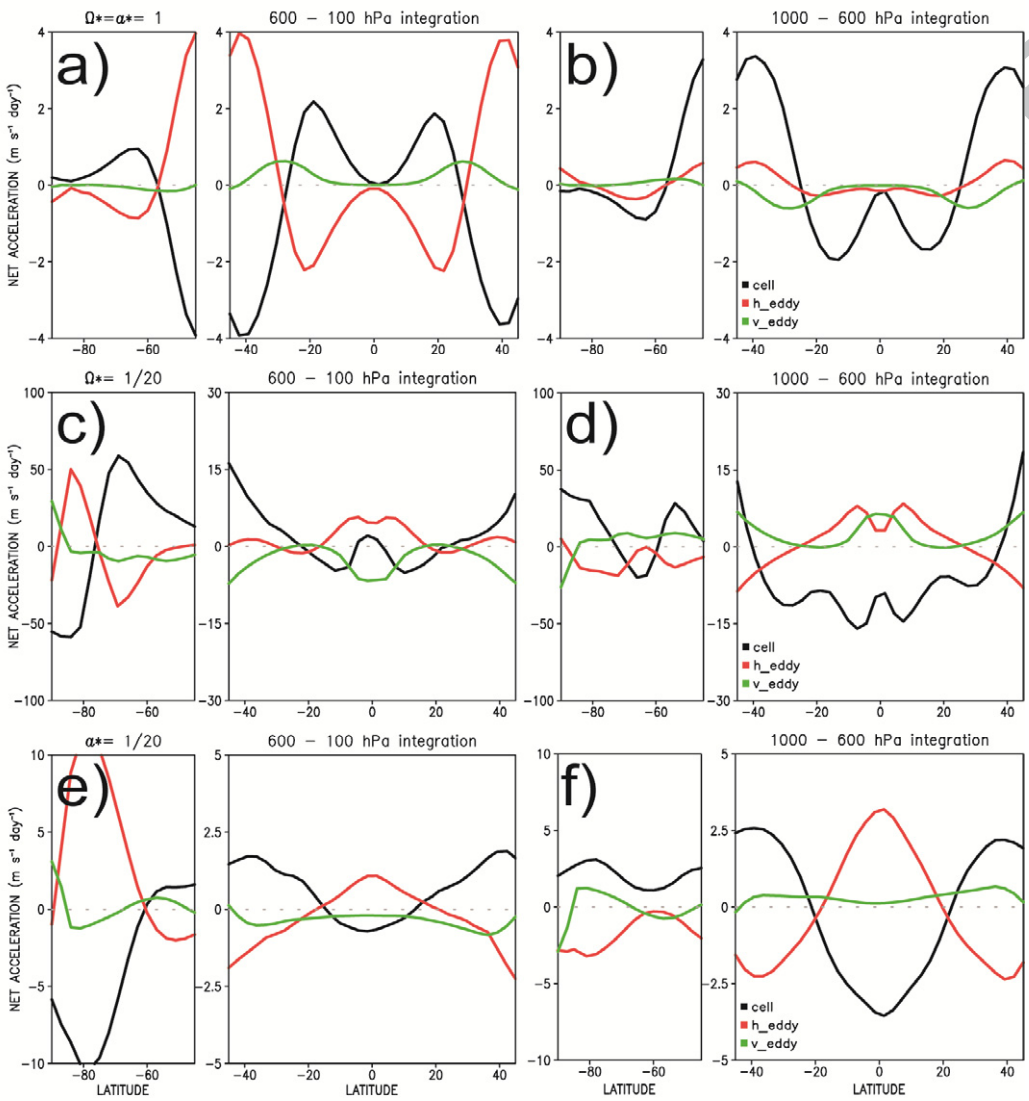

Figure 5. Vertically integrated net acceleration (in m s^{-1} day^{-1}) caused by the cells and the horizontal and vertical convergence of momentum by eddies: a) and b) for the Earth-like case experiment Ω*= *a**= 1; c) and d) for the Ω*= 1/20 experiment and, e) and f) for the *a**= 1/20 experiment. All the terms are integrated in the vertical in two layers: 1000 – 600 hPa and 100 – 600 hPa, and weighted by the atmospheric mass of the respective layer. Black lines indicate the terms related to the cells, red lines shows the eddy terms acting in the horizontal and the green lines, the eddy terms acting in the vertical.

In an Earth-like scenario the upper branch of the Hadley cell carries westerly momentum poleward from the equatorial region into the subtropics, thus accelerating the flow there (Figure 5a). Westerly momentum is transported by eddies and converges in midlatitudes in order to maintain the jets in these regions (see Peixoto and Oort, 1992; Schneider, 2006). The low-level equatorward branch of the Hadley cell carries easterly momentum toward the equator (Figure 5b). Due to instabilities in the jet regions, Rossby waves are produced and they propagate toward the subtropics and high latitudes, decelerating the flow (see Vallis, 2006; Randel and Held, 1991). These effects are strongest in the upper layer.

In the a^*, $\Omega^*= 1/20$ cases with higher Rossby numbers, the contrasting zonal mean wind structures (Figure 4c and 4e) between the experiments are reflected in different eddies and cells. For the slow-rotating experiment $\Omega^*= 1/20$, the cell term promotes strong acceleration of the zonal mean jets in the upper layer (i.e. the free troposphere of the model; Figure 5c and 4c). Since in this regime the Hadley circulation is wider (Figure 4d) these effects extend toward higher latitudes than in the Earth-like experiment. At polar latitudes where strong shear is present (Figure 4c), a Ferrel cell offsets eddy transports in a similar manner to the mid-latitudes in the Earth-like case. In the lower levels near the equator, small accelerations generated by the horizontal and vertical transport by eddies oppose the deceleration created by the low-level branch of the overturning circulation (Figure 5d). In the upper layers, vertical transport by eddies decelerate equatorial winds while horizontal eddy transport accelerates them.

For the smaller planetary radius experiment $a^*= 1/20$, in upper levels the cell decelerates the flow at the equator and accelerates it in mid- and subtropical latitudes, though the values are two orders of magnitude smaller than in the previous experiment (Figure 4d). At very high latitudes, where strong shear is present, the transport provided by the indirect Ferrell cell (Figure 4f) acts also to decelerate the flow. In contrast to the previous case, here

the vertical transport by eddies has relatively little influence on the momentum balance at the equator, and instead there is a balance between horizontal eddy transport accelerating (decelerating) the equator (subtropics) and the Hadley cell decelerating (accelerating) the equator (subtropics) at all levels. In this superrotating configuration (in steady state), the eddies transport more momentum where friction is present to sustain westerly flow against friction. In upper levels where the superrotation is well established, less is required from eddies to maintain the flow against the weak Hadley cell (see Saravanan, 1993; Mitchell and Vallis, 2010).

Our analysis shows that high value of Rossby number can yield two completely different states. While in the slow-rotating experiment there is the predominance of a strong jet in high latitudes, decreasing the radius instead produces intense and persistent westerly winds at the equator. The next section explores the origin of these differences based on the influence of other nondimensional parameters.

3.3. The influence of the rotation rate on the parametric regime

Estimates of the nondimensional numbers determined through the relations in the eqs. (4) – (5) are shown in Table 1 and the top of Figures 4a - 4f. The local Rossby number Ro (eq. 11) is shown in Figure 6 for our three simulations. An mean value was obtained by averaging in a layer between 200 – 400 hPa (i.e. at the jet levels) from |80°| to |10°| of latitude. Both $\Omega^*= 1/20$ and $a^*= 1/20$ simulations have a mean local Rossby number about two orders of magnitude larger than that of the Earth-like regime (0.02, see Figures 4 and Figure 6). Large *R*o indicates that the nonlinear acceleration in the advective terms (eq. 3) has comparable magnitude to the other terms, and thus, it cannot be neglected. When this happens the regime is no longer geostrophic and the cyclostrophic term becomes important.

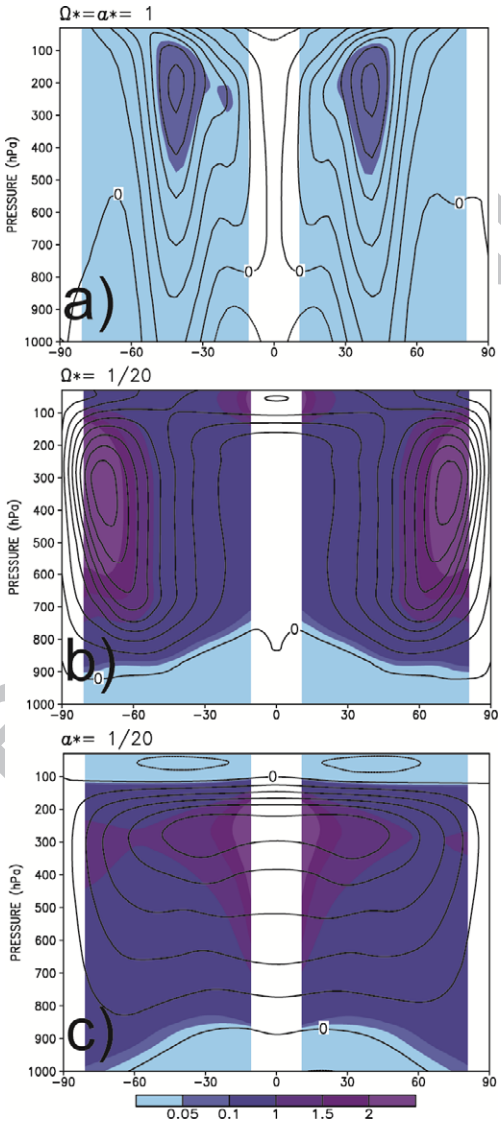

Figure 6. Local Rossby number (*Ro*) given by the time and zonal mean zonal wind (contour, each 10 m s^{-1}) for: a) the Earth-like case experiment Ω*= *a**= 1; b) for the slow rotating Ω*= 1/20 experiment and, c) for the smaller radius *a**= 1/20 experiment. Calculus was based on eq.11 and the values of the Table 1.

Besides the change in the Rossby number, other very important changes occur in the thermal and Ekman numbers. When the rotation rate is held fixed, and the planetary radius is reduced to induce a higher *R*o regime, the Ekman and thermal numbers, which do not depend on *a*, remain fixed compared to the Earth regime (Figure 4a and 4e). Thus both frictional and thermal characteristics, controlled by these two parameters, are not changed. However when the rotation rate is reduced, although a higher *R*o regime is achieved, the other parameters are also indirectly changed because they also depend on the planetary rotation rate. Therefore the modification in the rotation rate also alters the influence of friction in the boundary layer and changes the cooling and heating rates, i.e. the thermal properties, of the troposphere. If we recomputed the number as above for the experiment Ω*= 1/20, one would obtain an Ekman number 20 times bigger and a thermal relaxation coefficient 20 times smaller, which translates to 20 times stronger friction and heating/cooling rates. Read (2011) by computing the Taylor number, which is also a form of friction parameter, for the slow rotation experiments in Williams (1988a,b) paper pointed out that all these regimes were relatively strongly damped and therefore superrotation could not develop. With this high damping close to the surface, a consistent interpretation might involve kinetic energy extracted from the system, not allowing eddies to grow and evolve, and thus suppressing instabilities (James and Gray, 1986; Pascale et al., 2013).

Previous analysis has shown that the mean meridional circulation intensifies in the slow-rotating experiment, and the consequent suppressing of the superrotation. In order to test these ideas two extra experiments were run, Ω =1/20mod and Ω =1/20wkhd (see Table 1). Since the reduction of the rotation rate simultaneously modifies the three parameters, these experiments were performed in order to evaluate the impacts of offsetting the rotation rate variations in both Ekman E_k and thermal τ_a numbers. By definition E_k proportionally increases to the reduction of Ωwhereas τ_a decreases. Therefore these changes were offset by weakening

the friction and increasing the thermal relaxation time scale (i.e. leading to a higher thermal inertia) in the Held-Suarez forcing by the same factor.

Figure 7a depicts the modified version of the experiment Ω =1/20 (Ω =1/20mod), in which the intensity of both friction and Hadley cell are modified in order to offset the effects of the slower rotation rate in the nondimensional parameters. A comparison of the magnitude of these numbers as well as the spatial pattern of the zonal mean circulation shows that we have indeed reconstructed the results of the experiment a^*= 1/20 (Figure 4e). Such a behavior is a direct indication of the dynamical similarity between the two regimes, i.e. atmospheres that shares the same nondimensional numbers are dynamically equivalent and therefore they will exhibit the same statistical properties.

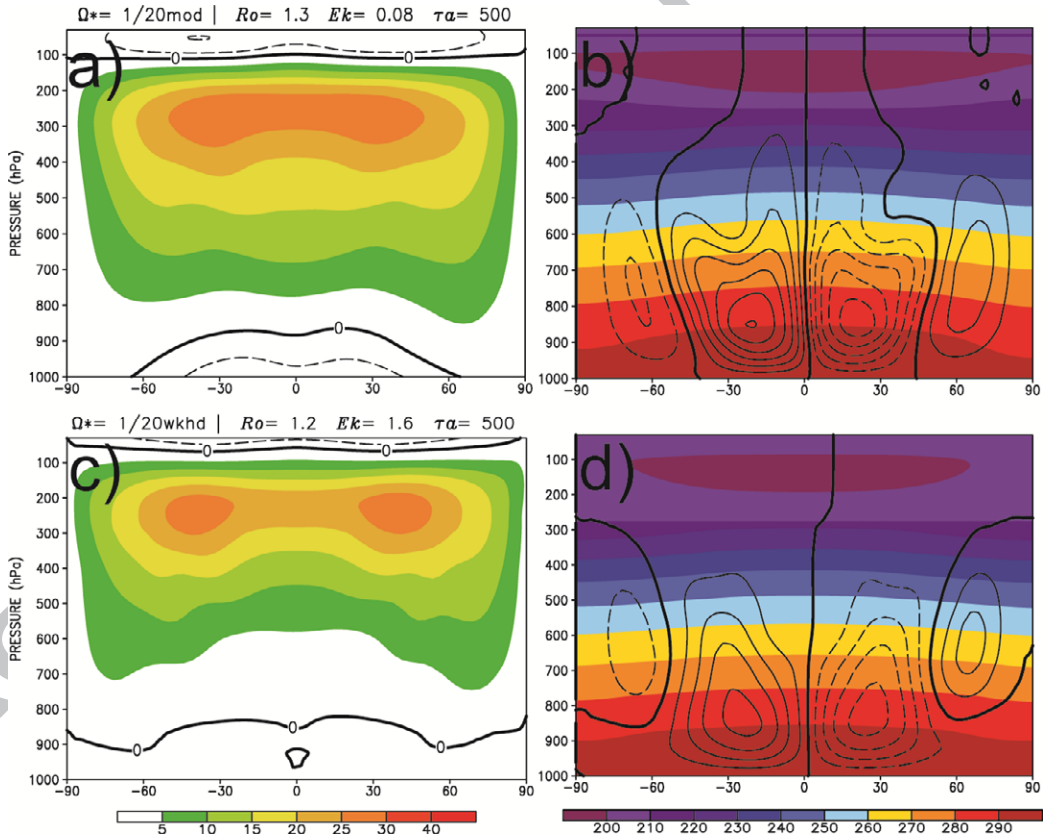

Figure 7. Vertical cross-sections of the time- and zonal-mean variables. The left panels are the zonal wind component (westerly winds in shaded; easterlies in dashed line with contour each 3 m s^{-1}). The right panels are temperature (shaded, K) and stream function ψ (contour, kg s^{-1}). a) and b) Experiment Ω*= 1/2mod (ψ contours each 5x10^9 kg s^{-1}); c) and d) Experiment Ω*= 1/20wkhd (ψ contours each 10x10^9 kg s^{-1}).The nondimensional parameters were computed based on the values in Table 1.

In order to evaluate which parameter is the most important to control the existence and intensity of the superrotation in the slow-rotating simulations, we performed the experiment Ω =1/20wkhd (*weaker Hadley*) in which only the intensity of the Hadley cell was changed. Thus the Ekman number remains the same as that of the experiment Ω =1/20 (Figure 4c), indicating intense friction at the model boundary layer. Figure 7c shows a hybrid wind pattern, with two jets in high latitudes but with substantial westerly winds in the equatorial region. This reinforces the importance of the mean meridional circulation intensity on the existence of the equatorial superrotation (Shell and Held, 2004), so that by only decreasing the Hadley cell strength the zonal winds pattern in the Figure 4c are substantially modified, giving rise to a new configuration depicted by the Figure 7c.

Figure 8 presents the wind profile of the zonal mean zonal wind at the jet level for the experiments a^*= 1/20, Ω =1/20 and Ω =1/20mod, [illegible], along with their associated potential vorticity, PV, and the hypothetical angular momentum conserving zonal wind, U_M. Both the a^*= 1/20 and Ω =1/20mod experiments are in a superrotating state. As we discussed above such a pattern requires a specific balance of accelerations between the meridional cells and transient eddies at the tropical region. For the experiment Ω =1/20, however, the zonal wind profile behaves as a nearly angular momentum conserving wind until around 60°, where the eddy accelerations start shifting the actual wind profile away from U_M. The low latitudes also have a very uniform PV distribution, as expected for angular momentum conservation. Therefore with a strong and dominant Hadley cell, the low-latitude circulation behaves as an axisymmetric one, in which an angular momentum maximum at the equator is not allowed to occur (Hide, 1969; Lindzen,1990).

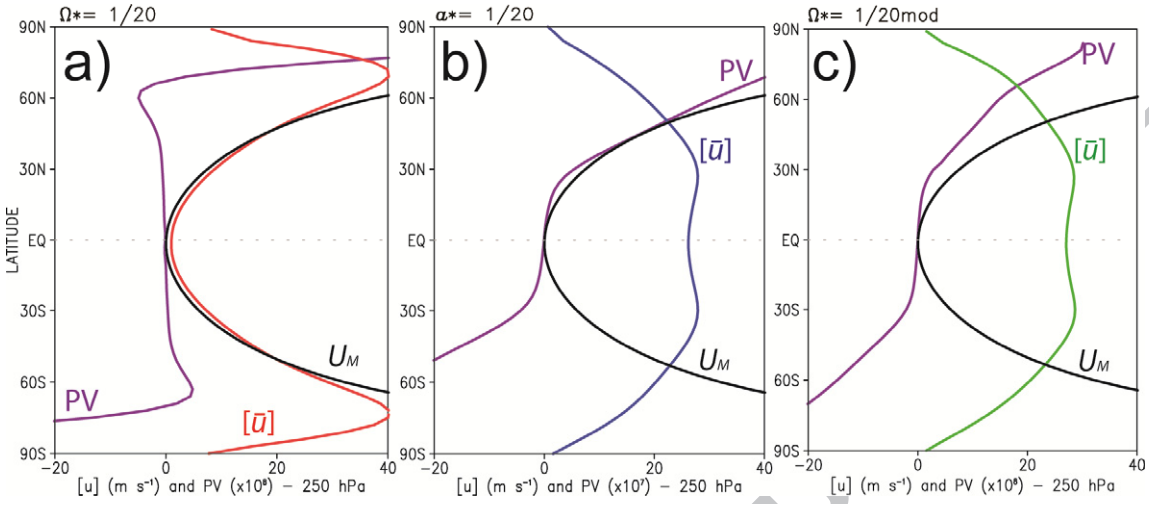

Figure 8. Zonal mean zonal wind profile (m s^{-1}) at 250 hPa for the experiments a^*= 1/20, Ω =1/20 and Ω =1/20mod. The black contour is the angular momentum conserving wind profile, computed as $V_M = \Omega a \frac{\sin^2\phi}{\cos\phi}$, where a is the planetary radius, Ω is the rotation rate and ϕ is the latitude. The purple contour is the potential vorticity. Values used for the computation are based on the Table 1.

3.4. Wave and eddies in the high *Ro* regime

It was argued that under a slow rotation regime, any structure of jet in the zonal flow should be barotropically unstable (Rossow and Williams, 1979) and therefore, propagating modes triggered by the unstable jet in high latitudes could propagate toward to the equatorial region inducing convergence of momentum necessary to maintain the winds there (which is the basis of the GRW mechanism; see Del Genio and Suozzo, 1987; Del Genio et al., 1993; Hourdin et al., 1995; Del Genio and Zhou, 1996; Williams, 2003; Luz and Hourdin, 2003; Lebonnois et al., 2010). However, based on fundamental properties of linear Rossby waves (see Held, 1999; Vallis, 2006 for example), such a propagation (here is considered Rossby-waves as the planetary disturbances) toward the equator as described above would lead to deceleration in that region, or in other words divergence of momentum.

In order to distinguish which mode contributes toward momentum convergence (acceleration) at the equator, we regressed the geopotential height and wind fields onto the Empirical Orthogonal Functions (EOF, known also as Principal Component Analysis PCA) from the zonally asymmetric component of the geopotential height. EOFs are widely used in meteorology and they are derived as the eigenvalues and eigenvector from a covariance (or correlation) matrix (see Lorenz, 1956; North, 1984; Hannachi et al., 2007). The first few EOFs (i.e eigenvectors) and the associated eigenvalues are interpreted as natural modes of variability and their spatial patterns. Propagating wave-like oscillations, for instance, are represented by the EOFs analysis as a pair of eigenvectors with similar eigenvalues, and the associated spatial patterns are shifted by a quarter of wavelength. We perform the EOF analysis at two different vertical levels: one where the *convergence of momentum at the equator* was maximum, and the second one at higher levels where *the zonal mean winds* were strongest.

Here we are presenting the analysis for the Ω =1/20, a^* =1/20 and Ω =1/20mod experiments. Figure 9 shows the vertical cross section of the time- and zonal-mean eddy acceleration (related to the convergence of the momentum transport, see eq. 9), the zonal-mean wind and a line indicating the levels where the EOF analysis was applied. Figure 10 – 11 depicts the main variability modes of the geopotential height and winds at these lower- and higher-levels and the acceleration associated with the EOFs. The first four EOFs for each experiment, which roughly correspond to 90% of the explained variance of the data, were grouped into two groups with the same spatial characteristics and similar variance, thus indicating two distinct, spatially propagating modes.

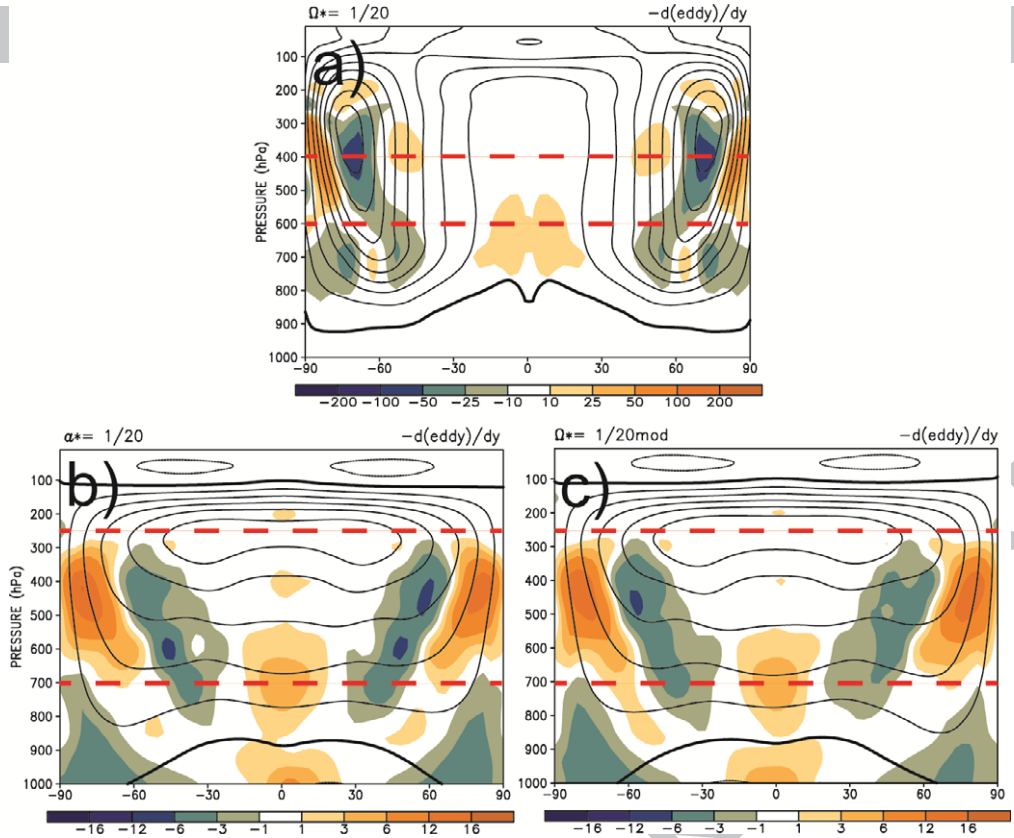

Figure 9. Vertical cross section of the zonal mean convergence of momentum by the eddy transients $-\frac{1}{a\cos^2\phi}\frac{\partial}{\partial\phi}\left(\cos^2\phi\,\overline{u^*v^*}\right)$ (shaded, in m s^{-1} day^{-1}) and zonal mean zonal wind (contour with a bold line for zero values, m s^{-1}) for: a) Ω =1/20, b) a^* =1/20 and, c) Ω =1/20mod experiments. The red dashed lines indicate the levels from which the anomalies of geopotential were taken to perform the EOF analysis.

Although acceleration at the lower troposphere of the equatorial region is observed for the experiment Ω =1/20 (Figure 9a), the eddies are confined in the regions of intense meridional wind shear close to the jets in the very high latitudes (as previously observed in Figure 4c) where non-homogeneous PV is created (Figure 8a). In this experiment, the general circulation behaves as if it is nearly axisymmetric and the Hadley cell dominates momentum transport (Figure 5c), such that superrotation does not develop. Thus simulations under high *Ro* and strong damping (see section 3.3) would generate axisymmetric circulations without any significant eddy activity and superrotating jets (Geisler et al., 1983) at the equatorial region, which was indeed observed in the experiment Ω =1/20.

The two modes in the geopotential height anomalies (taken at 400 and 600 hPa) are depicted in Figure 10a and 11a. They are basically composed by high latitude perturbations

associated with instabilities generated by strong meridional wind shear on the poleward flanks of the jets. The 1st group (representing more than 80% of the explained variance of the anomalies of geopotential height) is a zonal-wavenumber-one wave whose phase is shifted 180° between the hemispheres (Figure 10a and 11a) and tilts with latitude in both lower- and higher-levels. Such a horizontal structure is characteristic of a $n = 0$ mixed Rossby-gravity-like wave (see Figure 3c from Kiladis et al., 2009) with a barotropic vertical structure. This mode is responsible for the acceleration patterns shown by Figure 9a, generating small acceleration at the equatorial region at 600 hPa and strong deceleration in high latitudes at 400 hPa. The 2nd group (roughly representing 12% of the explained variance) is composed by a wavenumber one Rossby wave (in phase between the hemispheres), and it does not exert equatorial accelerations on the equator.

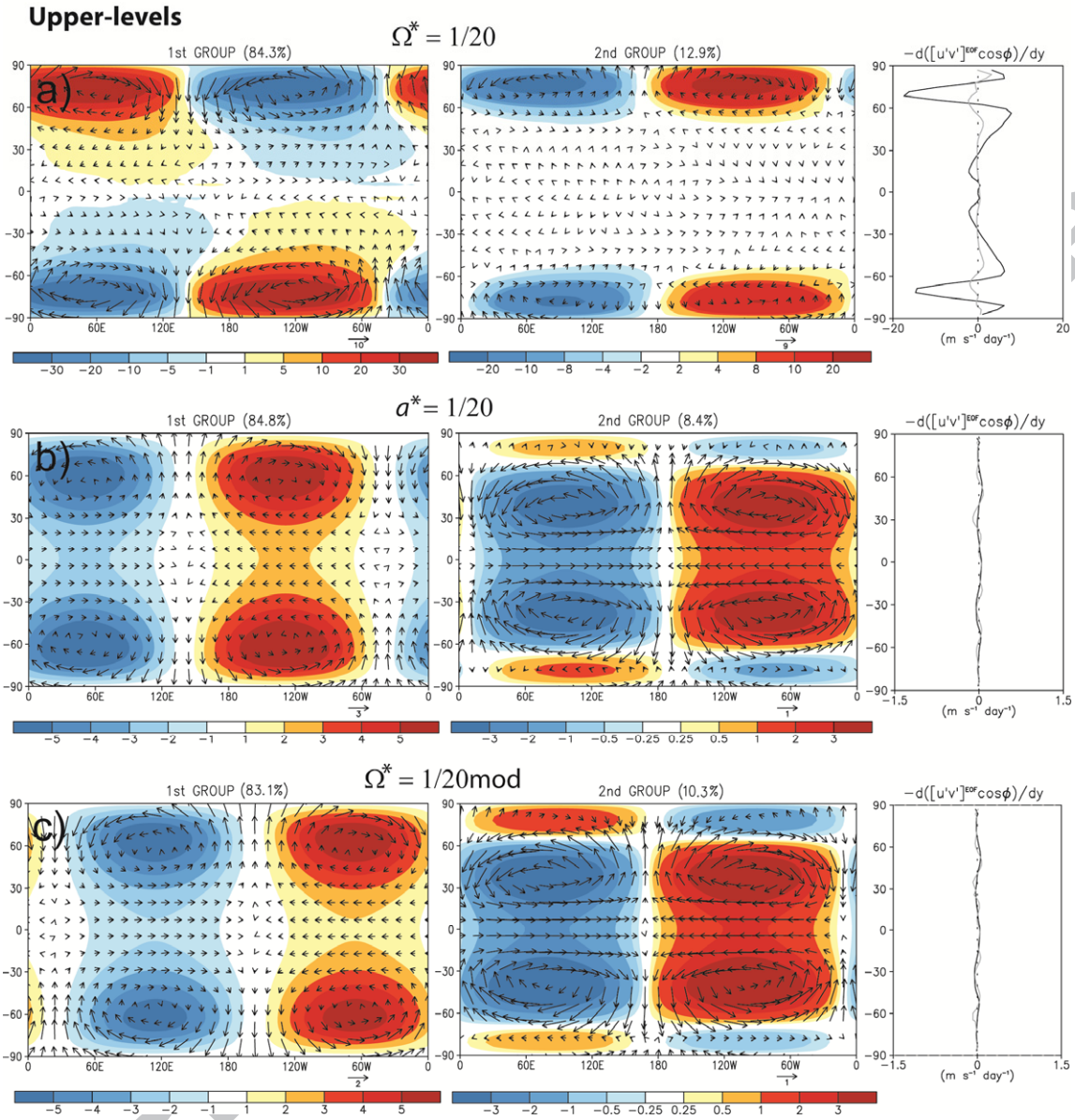

Figure 10. Variability patterns of geopotential height (shaded, m) and horizontal wind (vector, m s^{-1}) associated with the EOFs for: a) experiment Ω =1/20 at 400 hPa, b) experiment a^* =1/20 at 250 hPa and, c) experiment Ω =1/20mod at 250 hPa. Convergence of momentum by each group of modes is also depicted in the panels on the right (black lines for 1st group and grey lines for the 2nd group, m s^{-1} day^{-1}). The percentage refers to the sum of the explained variance of the EOFs related to that mode.

In a superrotating cases, however, a completely different wave pattern emerges. The vertical cross section (Figures 9b and 9c) of time mean accelerations show the eddies have considerable effects in all equatorial troposphere below 500 hPa with peak aroud 700 hPa,

which is the region close to the boundary layer of the model. Above this region at the equator, the time-mean momentum convergence practically vanishes. The pattern of acceleration and deceleration between 60° S – 60° N reinforces the existence of a wider wave guide with eddy source at the equator to promote acceleration of the zonal flow there and deceleration at the flanks. Other regions of acceleration (with maximum between 400 – 500 hPha) are closely related to the meridional wind shear at the high latitudes as in the previous experiment.

Both in the reduced radius and in the modified slow-rotating experiment, the presence of strong and persistent westerly winds in the equatorial region is accompanied by the same two wave modes (Figure 10 and 11b,c). The 1st group shows pairs of cyclones and anticyclones in high latitudes with unit zonal wavenumber. The geopotential anomalies associated with these planetary-scale Rossby waves are stronger in higher levels although the waves have a barotropic structure with the alignment of cyclones and anticyclones in height. The acceleration/deceleration in the 1st group is located poleward of 30° in lower-levels of the atmosphere.

The 2nd group, although less important to the explained variances (i.e. patterns more transient in time), is the most important source of momentum convergences at the equator (b and c plots in Figures 9, 10 and 11). It is composed of a pair of wavenumber-one equatorial waves coupled with high latitude waves with a shift of around 180° between their phases. The spatial pattern resembles that observed in equatorial Rossby waves $n = 1$ from Matsuno's theory, consisting of a quadrupole of streamfunctions anomalies of opposite signs, symmetric about the equator giving rise to the characteristic "cyclone/anticyclone" pairs (Wheeler and Kiladis, 1999) with an extratropical projection. Differently from 1st group, the vertical structure has strong variation, with the equatorial wave more intense and meridionally wider in higher levels than its extratropical counterpart, thus indicating that the 2nd group is a baroclinic mode. Consistent with the baroclinic structure, the latitudinal tilting in their phase

lines at 700 hPa indicates momentum transport from higher to lower latitudes (grey lines in the acceleration plots). The wave guide of the equatorial Rossby wave, between 30° S and 30° N at 700 hPa and 60° S and 60° N at 250 hPa, reflects the meridional extension of the acceleration and decelerations described above within the same range of latitudes.

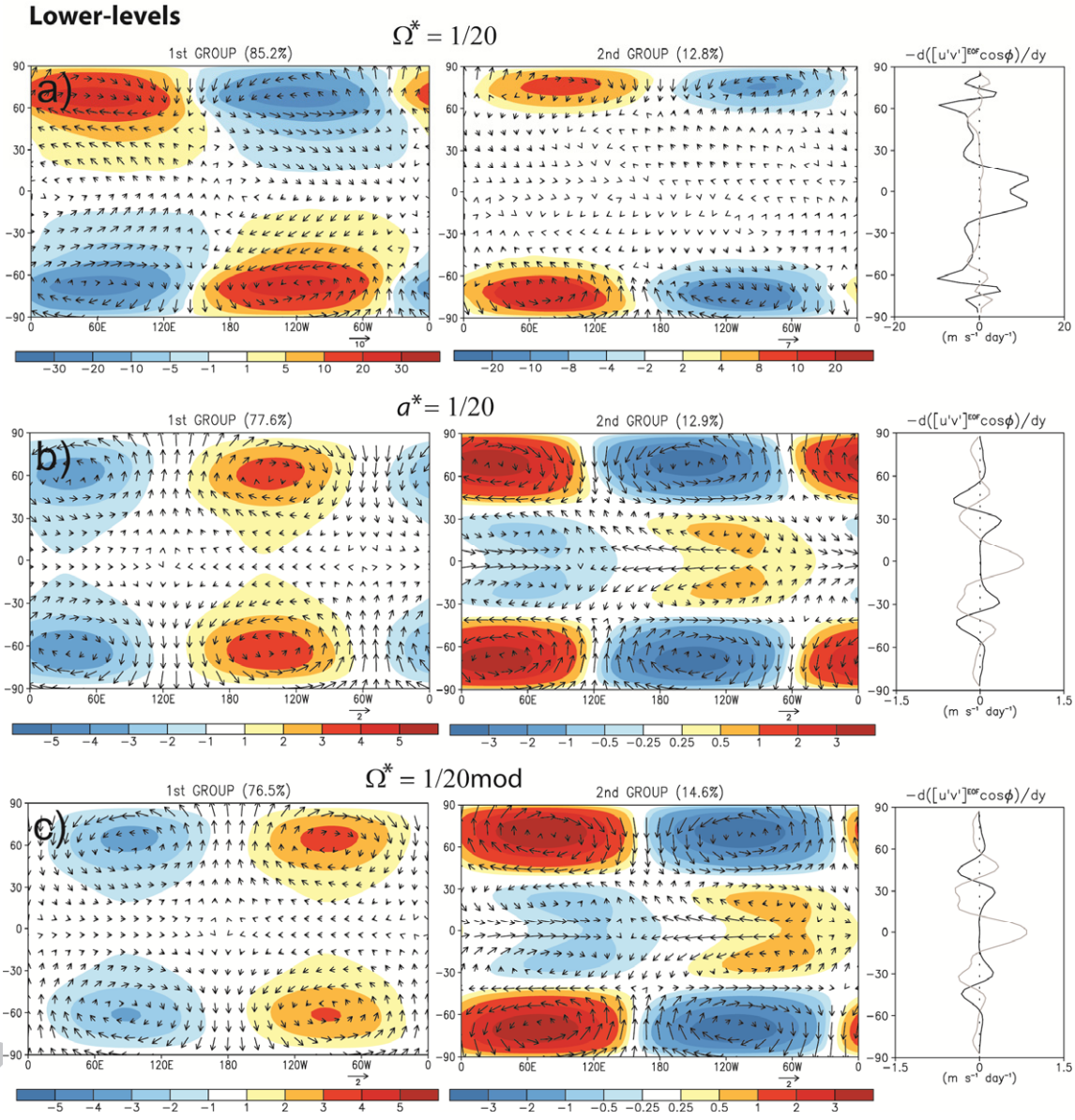

Figure 11. Variability patterns of geopotential height (shaded, m) and horizontal wind (vector, m s^{-1}) associated with the EOFs for: a) experiment Ω =1/20 at 600 hPa, b) experiment *a** =1/20 at 700 hPa and, c) experiment Ω =1/20mod at 700 hPa. Convergence of momentum by each group of modes is also depicted in the panels on the right (black lines for 1st group and grey lines for the 2nd group, m s^{-1} day^{-1}). The percentage refers to the sum of the explained variance of the EOFs related to that mode.

Mitchell and Vallis (2010) noticed in their idealized experiments that when *R*o exceeded unit, a global scale wavenumber one eddy response arose converging momentum in the equatorial region and inducing superrotation. The main mode found by the authors was basically composed by high latitude Rossby waves and a well-developed off-phase Kelvin wave ("the chevron" mode). Such a coupling of Kelvin and Rossby waves has also been reported in other theoretical studies, as for example Iga and Matsuda (2005, Figure 16), Yamamoto and Takahashi (2006, Figure 14) and Potter et al. (2014, Figure 16).

On the other hand, some studies imposing anomalous heat sources in the equatorial region for the Earth's Rossby number regime found a global scale eddy response (for example Figure 3c in Kraukunas and Hartmann, 2005, and Figure 3b in Arnold et al., 2012) with anticyclones flanking the equator upstream of the heating source and cyclones downstream (with structure similar to the 2nd group obtained in Figure 10 and 11b,c) and with tilted phase lines so that momentum could be transported toward to the equator (Caballero and Huber, 2010). The novel results of this study suggest that the spontaneous, i.e. not dynamically forced, convergence of momentum to the equator in our higher Rossby number regime involve this same kind of wave structures. This may indicate that not only more dynamical paths are possible but also that different modes could be candidates to produce and/or sustain superrotation in the model.

3.5. Dynamical origin of the modes from experiment $a^* = 1/20$

In this section we briefly explore some possible origins of the modes present in the experiment $a^* = 1/20$. Spectral analysis was applied in order to identify the main frequencies of oscillation of the modes described in the last section. Power spectra of the zonal wind anomalies (not shown) indicates there are two main frequency bands: the 1st group is a slower mode with frequency around $0 < \omega < 0.1$ cycles-per-day; whereas the faster 2nd group has a

frequency lying $0.4 < \omega < 0.6$ cycles-per-day. Figure 12 shows the time series of the geopotential height at 250 hPa filtered to only retain the two bands above. Based on the horizontal structure of the waves in Figure 10b we identified the latitude of the grid point closest to maximum amplitude of the waves (for both the longitude was arbitrarily chosen to be 0°).

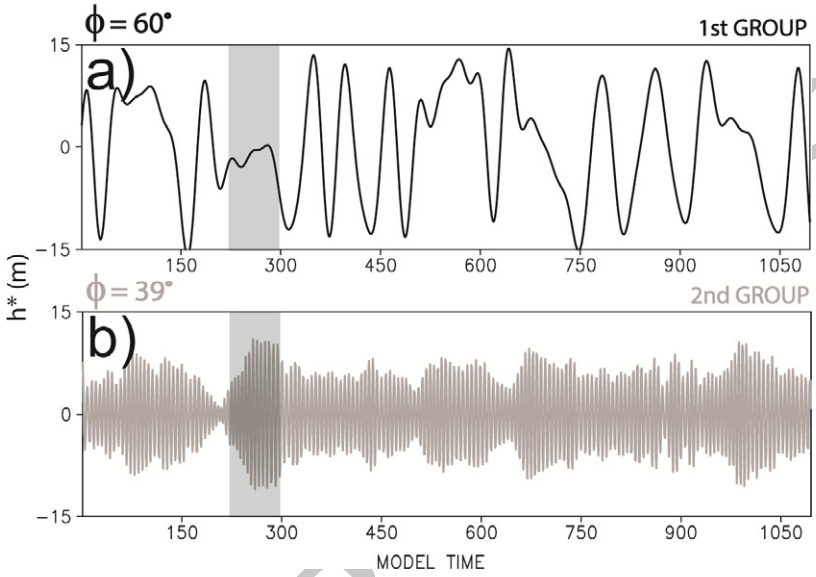

Figure 12. Time series of the geopotential height anomalies (contours, m) at 250 hPa filtered in the frequency bands of the two dominant modes present in the experiment $a^* = 1/20$. a) 1st group, taken at latitude of 60° and b) 2nd group, taken at latitude of 39°. Both longitudes were arbitrarily chosen to be 0°. The area highlighted in grey was used to compute the meridional PV gradient and potential temperature in Figure 13b.

Apart from the natural oscillation of each mode, there are modulations of the amplitude of these oscillations. When 1st group has minimum in amplitude, the 2nd group obtains slightly higher amplitude (highlighted area in grey, for example, on Figure 12a and 12 b). This coordinated behavior might indicate some interaction between these two modes and will be investigated in a companion paper. The role of both barotropic and baroclinic instabilities, however, acting in the maintainance of the superrotation during the steady state is explored in Figure 13. According to Vallis (2006) and Mitchell and Vallis (2006) the presence of the barotropic and baroclinic instabilities is identified through the spatial distribuition of the meridional gradient of the zonal-mean potential vorticity ($\partial[\overline{PV}]/\partial y$).

When meridional gradient of absolute vorticity (also PV) changes sign in the absence of horizontal gradient of potential temperature, there are conditions favorable for barotropic instability, whereas changes in sign of meridional gradient of PV indicates condition favorable for baroclinic instability in the presence of horizontal gradient of potential temperature.

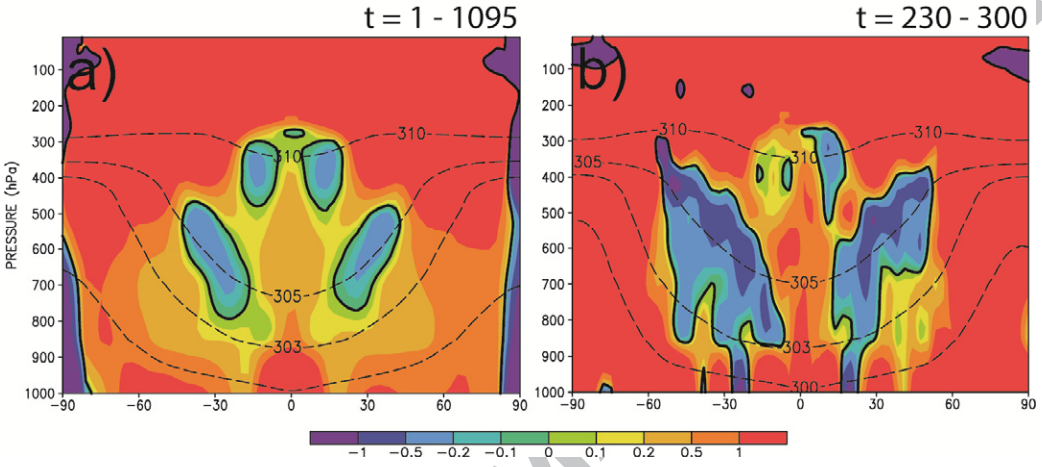

Figure 13. Vertical cross section of time- and zonal-mean potential vorticity gradient (shaded, x10^{12}) and potential temperature (dashed lines, K) for the experiment a^* = 1/20. a) values averaged over the entire period, b) values averaged from model time 230 to 300, which is roughly represented by the grey box in Figure 12.

When averaged over the entire analysis period of the simulation (Figure 13a), it is clear that there are several regions of PV reversal in the troposphere. At very high latitudes the abrupt change in signal of $\partial[\overline{PV}]/\partial y$ indicates a possible the role for barotropic instability at these regions, which is confirmed by the existence of the slow-propagating barotropic Rossby waves (1st group, see Figures 10b and 11b). Near the subtropical latitudes, PV gradient reverses sign in the presence of potential temperature gradient, which is confirmed by the existence of the fast-propagating baroclinic equatorial Rossby-waves from the 2nd group. There is also reversal of the PV gradient in low levels at the equatorial region, which may indicate a mixed barotropic-baroclinic instability as argued in Mitchell and Vallis (2010).

As mentioned before, during the periods of weak amplitude oscillation of 1st mode, the amplitude mode from the 2nd group grows. One of these periods is displayed in Figure 13b.

The high latitude PV gradient reversal vanishes whereas abrupt and strong vertical variation in the lower-level PV gradient is observed. This behavior along with a bigger slope of the 300 K isothermal contour indicates stronger role of the baroclinic instability at this short periods. Therefore there is a mix in average of the barotropic and baroclinic instabilities acting in the troposphere, but there is a clear distinction between the modes and each related instability.

3.6. Analysis of the spin-up period of the model

Motivated by the fact that different wave modes could be responsible for the generation and maintenance of the superrotation in a high Rossby number atmosphere as the literature suggests, here we present an analysis of the spin-up of the simulation $a^* = 1/20$.

Figure 14a shows the vertical cross section of the time evolution of the zonal mean zonal wind [u] averaged between 15º S – 15º N latitudes, from the initial axisymmetric phase to the establishment of superrotation. Westerly winds are initially generated in the upper atmosphere near 200 hPa, but rapidly extend to 600 hPa by day 150. A gradual increase in the wind intensity between 400 – 200 hPa occurs until time 500. This is followed by an abrupt adjustment phase leading to the steady-state configuration after time 600. Since eddy disturbances are necessary for the convergence of momentum at the equator, Figure 14b depicts the instantaneous accelerations within the same region (15º S – 15º N) due to the horizontal momentum convergence by the eddies.

Two distinct regimes are also noted for the same period of Figure 14a. In the first one, which is active from time 150 until around time 500, the level of maximum acceleration is around 600 hPa with only sporadic episodes in levels above and below. Between times 500 and 600, the period of abrupt downward shift of the westerly wind layer, the level of maximum acceleration also shifts to 700 hPa (roughly tracking where the velocity of the wind

was around 5 – 10 ms^{-1}). In the steady state, the maximum of the eddy acceleration remains around 1000 and 700 hPa (see also Figure 9b).

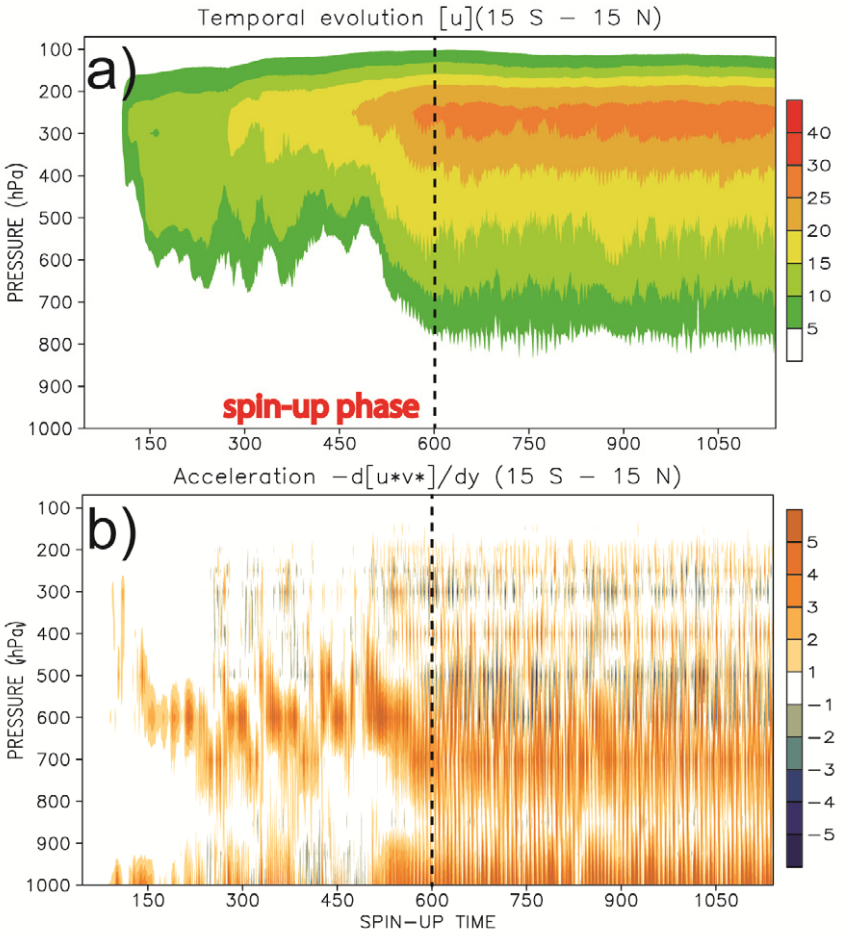

Figure 14. Vertical cross section of the time evolution of the: a) zonal mean zonal wind component (m s^{-1}) and b) instantaneous acceleration due to eddies (m s^{-1} day^{-1}). Both variables are averaged between 15º S and 15º N latitudes. The dashed line indicated the approximated time that divides the spin-up and the steady state of the simulation.

As already shown in the steady state analysis, the areas of most intense eddy momentum convergence do not correspond to the level of wind maximum (~ 250 hPa). However, studying the levels where eddy convergence is present reveals which modes contribute to the maintenance of superrotation. Given the transient state and fast evolution of the quantities during the spin-up, an EOF analysis is problematic, and thus we opted to show

snapshots of the zonally asymmetric components, filtered for wavenumber one, during the generation of superrotation.

Figure15 shows snapshots of the zonally asymmetric component of wind and geopotential filtered for wavenumber one, and the zonal mean of their instantaneous acceleration. The selected periods are roughly related to times of maximum acceleration in 600 hPa. During the gradual evolution of the wind field, between times 150 and 500, the anomalies are very close in shape to the wavenumber one Kelvin- and Rossby-like waves (Figure 15a, 15b and 15c). These high latitude Rossby-like waves are coupled to an equatorial Kelvin-like wave. Although the signature of the equatorial Kelvin wave is weaker, the patterns related to positive and negative anomalies of geopotential and the winds match those found in a pure Kelvin wave n = -1, obtained from the shallow-water solutions of Matsuno (1966) (see Figure 3f from Kiladis et al., 2009). The positive geopotential anomalies are associated with eastward zonal flow whereas the negative ones are associated with westward zonal flow, and the zonal flow associated with this Kelvin wave decays away from the equator. The building-up of persistent westerly equatorial winds during this period is due to the coupling of these modes, as described in Mitchell and Vallis (2010) and Potter et al. (2014).

After time 429, the abrupt transition occurred leading to another regime in which, as shown by Figure 15d, equatorial Rossby-like waves accelerate the equatorial winds. It is just after this period that superrotation is fully established in whole troposphere. Afterwards the accelerations are no longer intense and persistent at 600 hPa, and the eddy field is dominated by a Rossby-like mode similar to those found in the 2nd group of the steady state (Figures 10c, 15e and 15f). Such an evolution indicates that the formation and existence of the Rossby-Kelvin-like coupling is crucial to the onset of persistent westerly winds over the equator,

while Rossby-Rossby-like coupling promote expansion of westerly equatorial winds through the depth of the troposphere and maintain superrotation through the steady state.

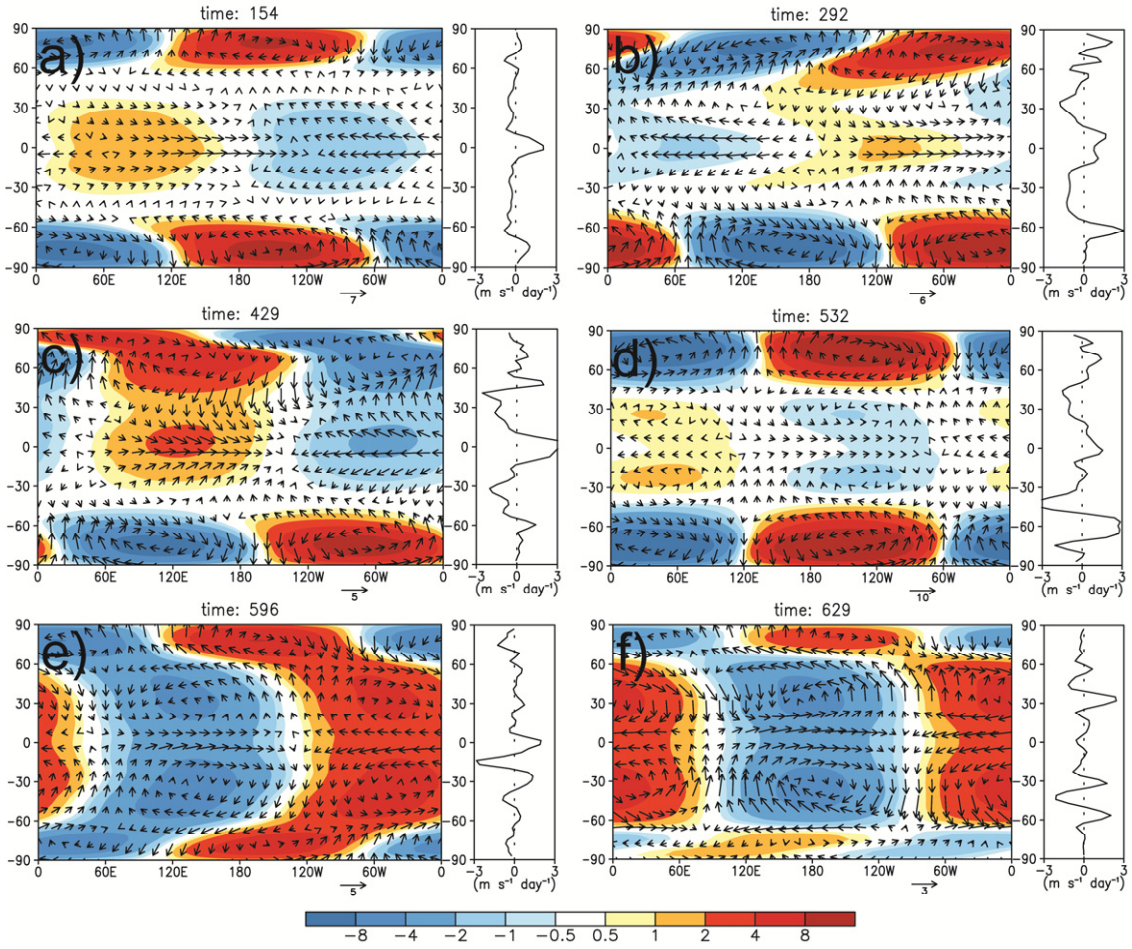

Figure 15. 600 hPa geopotential anomalies (shaded, m), wind (vectors, m s^{-1}) and instantaneous accelerations (contours, m s^{-1} day^{-1}) at different instants during the spin-up of the simulation $a^* = 1/20$: a) time 154, b) time 192, c) time 429, d) time 532, e) time 596, and f) time 629. The selected period refer roughly to the times of maximum acceleration in Figure 14b.

4. Concluding remarks

In this study, superrotation in the context of higher Rossby number atmospheres was studied by performing numerical simulations with a simplified Earth-like GCM set for either a slow rotation rate or a reduced planetary radius. Substantial differences in strength and zonal mean pattern of the zonal winds were found when running the model with a slow

rotation rate, which is the traditional approach, and a smaller planetary radius. By analysis of the simulations, we elucidated the key elements inhibiting superrotation in slowly rotating Earth-like GCMs.

When set to a slower rotation rate, the model generated an almost axisymmetric circulation, with strong jets in the very high latitudes and wider Hadley cells. The transport of momentum was due basically to the strong mean meridional circulation that diverges momentum from the equatorial region and brings it into the high latitudes feeding the jets. Any convergence of momentum at the equator does not overcome the effects of the strong Hadley cell. Our simulation with a reduced planetary radius, on the other hand, develops robust superrotation, produces a nearly barotropic thermal structure, i.e., lacking strong latitudinal temperature gradients, in almost all troposphere and has a very weak mean meridional circulation with momentum transport very similar in magnitude to the eddy transport. Differently from the slowly rotating experiment, stronger convergence of momentum is produced in a large part of the lower troposphere, where the effects of the friction are present. The momentum convergence practically vanishes in the upper troposphere in the steady state. A small, vertical transport of momentum is provided by the mean meridional circulation. In the strongly superrotating levels aloft, on the other hand, the lack of forcing by eddies indicates that little is required to maintain the zonal flow, in contrast to the lower levels where stronger dissipation from Rayleigh friction is present. In the steady state, two dynamically active modes are dominant. The first one is a slow-propagating, barotropic, high-latitude Rossby wave and causes acceleration just in higher latitudes. The second one is a fast-propagating, baroclinic, equatorial Rossby-like wave with an extratropical projection and it is responsible for all convergence of momentum at the equator. Although the 1st mode is not responsible for the maintenance of the superrotation, its interaction with 2nd mode seems important in short and transient periods of time. For the spin-

up phase, on the other hand, it is the Rossby-Kelvin coupling that is responsible for the onset of the superrotation.

Our analysis showed that superrotation could only emerge in a planet of slow rotation rate if the damping was weak and the thermal time scales in the atmosphere were long enough (i.e a long thermal inertia). Thus when the rotation rate is reduced, our model generated a nearly axisymmetric circulation with intense Hadley cells, which prevent the development of superrotation. Therefore, a large Rossby number is a necessary condition but not sufficient one to achieve superrotation; Hadley cell intensity seems also to be important. These conditions can be evaluated by estimating nondimensional numbers, even for more complex models. Interestingly, simulations with different dimensional parameters but the same nondimensional numbers share the same behavior of mean general atmospheric circulation, and therefore a GCM satisfies the principle of dynamical similarity. Superrotation should not be thought of as a phenomenon that only occurs on slowly rotating planets, since for instance superrotation could be also present on fast-rotating planets if they are sufficiently small.

Our analysis also demonstrated the possibility of different wave combinations that generate superrotation, indicating that multiple paths could be possible to produce such a flow. Further model inter-comparison may help to illuminate this variety of waves that participate in generating and maintaining spontaneous superrotation. Additionally many aspects of the interaction between waves and the mean flow under a high Rossby number regime remain unclear. Since quasi-geostrophic theory cannot be applied in such systems, traditional ideas about mid-latitude instabilities cannot be used as well. The potential interaction between different distinct waves and the effects in the mean flow will be investigated in a companion paper. Further study of equatorial waves in the Venus and Titan

atmospheres is also needed, especially observations that allow the identification of wave patterns in their upper and lower atmospheres.

Acknowledgements

The authors would like to acknowledge financial support from FAPESP (Grants 2012/13202-8 and 2010/15174-6), NASA PATM (Grant NNX12AI71G), and UCLA's Institute for Planets and Exoplanets (iPLEX). The authors would like to thank Dr. Peng Wang, Dr. Salvatore Pascale and the anonymous reviewers for all suggestions that helped to improve the manuscript. This research was conducted through the Visiting Graduate Researcher program of the University of California and it is part of the Ph.D. thesis of the first author.

5. References

Arnold, N. P., E. Tziperman, and B. Farrell (2012), Abrupt Transition to Strong Superrotation Driven by Equatorial Wave Resonance in an Idealized GCM, *J. Atmos. Sci*, **69**, 626–640.

Bird, M. K., M. Allison, S. W. Asmar, D. H. Atkinson, I. M. Avruch, R. Dutta-Roy, Y. Dzierma, P. Edenhofer, W. M. Folkner, L. I. Gurvits, D.V. Johnston, D. Plettemeier, S.V. Pogrebenko, R. A. Preston, and G. L. Tyler (2005), The vertical profile of winds on Titan. *Nature*, **438**, 800–802.

Bougher S. W., D. M. Hunten, and R. J. Phillips (1997), *Venus II – Geology, Geophysics, Atmosphere and Solar Wind Environment*. The University of Arizona Press, 1362 pp.

Caballero, R., and M. Huber (2010), Spontaneous transition to superrotation in warm climates simulated by CAM3, *Geophy. Res. Lett*., **37**, L11701.

Del Genio, A., and R. J. Suozzo (1987), A comparative study of rapidly and slowly rotating circulation regimes in a terrestrial general circulation model. *J. Atmos. Sci*., **44**, 973–986.

Del Genio, A.D., W. Zhou, and T.P. Eichler (1993), Equatorial superrotation in a slowly rotating GCM: Implications for Titan and Venus. *Icarus*, **101**, 1–17.

Del Genio, A.D., and W. Zhou (1996), Simulations of superrotation of slowly rotating planets: Sensitivity to rotation and initial condition. *Icarus*, **120**, 332–343.

Eady, E. (1949), Long waves and cyclone waves. *Tellus*, **1**, 33–52.

Flasar, F. M., K. H. Baines, M. K. Bird, T. Tokano, and R. A. West (2009), Atmospheric Dynamics and Meteorology. In: "*Titan from Cassini-Huygens*". Edited by R. Brown, J. P. Lebreton and J. Hunter Waite, Chap. 13, 323–352.

Friedson, A. J., R. A. West, E. H. Wilson, F. Oyafuso, and G. S. Orton (2009), A global climate model of Titan´s atmosphere and surface. *Planet. Space Sci*, **57**, 1931–1949.

Geisler, J.E., E.J. Pitcher, R.C. Malone (1983), Rotating-fluid experiments with an atmospheric general circulation model. *J. Geophys. Res*., **88**, 9706–9716.

Gierasch, P. J. (1975), Meridional Circulation and the Maintenance of Venus Atmospheric Rotation, *J. Atmos. Sci*, **32**, 1038–1044.

Hannachi, A., I. T. Jolliffe, and D. B. Stephenson (2007), Empirical orthogonal functions and related techniques in atmospheric science: A review. *International Journal of Climatology*, **9**, 1119–1152.

Hide, R. (1969), Dynamics of the Atmospheres of the Major Planets with an Apendix on the Viscous Boundary Layer at the Rigid Bounding Surface of an Electrically-Conducting Rotating Fluid in the Presence of a Magnetic Field. *J. Atmos. Sci*, **26**, 841–853.

Held, I. M. and A. Y. Hou (1980), Nonlinear axially symmetric circulation in a nearly inviscid atmosphere. *J. Atmos. Sci*, **35**, 515–533.

Held, I. M and M. J. Suarez (1994), A proposal for intercomparison of the dynamical cores of Atmospheric general circulation models. *Bull. Amer. Meteo. Soc*., **75**, 1825–1830.

Held, I. (1999), *Equatorial Superrotation in Earth-like Atmospheric Models*. Bernhard Haurwitz Memorial Lecture, American Meteorological Society.

Holton, J. R. (2004), *An Introduction to Dynamic Meteorology*. 4th Edition, Elsevier Academic Press, New York. 535 pp.

Hollingsworth J. L., R. E. Young, G. Schubert, C. Covey, and A. S. Grossman (2007), A simple-physics global circulation model for Venus: Sensitivity assessments of atmospheric superrotation. *Geophy. Res. Lett*., **34**, L05202.

Hourdin, F., O. Talagrand, R. Sadourny, R. Courtin, D. Gautier, and C. P. McKay (1995), Numerical simulation of the general circulation of the atmosphere of Titan. *Icarus,* **117**, 358–374.

Hunt, B. G. (1979), The influences of the Earth's rotation rate on the general circulation of the atmosphere. *J. Atmos. Sci*, **36**, 1392–1408.

Iga, S.-I., and Y. Matsuda (2005), Shear Instability in a Shallow Water Model with Implications for the Venus Atmosphere. *J. Atmos. Sci*, **62**, 2514–2527.

James, I. (1994), *Introduction to Circulating Atmosphere*. Cambridge University Press. 422 pp.

James, I. and L. Gray (1986), Concerning the effect of surface drag on the circulation of a baroclinic planetary atmosphere. *Quarterly Journal of The Royal Meteorological Society*, **112**, 1231–1250.

Kiladis, G. N., M. C. Wheeler, P. T. Haertel, K. H. Straub, and P. E. Roundy (2009), Convectively coupled equatorial waves. *Reviews of Geophysics*, **47**, RG2003.

Kostiuk T., K. E. Fast, T. A. Livengood, T. Hewagama, J. J. Goldstein, F. Espenak, and David Buhl (2001), Direct measurement of winds on Titan. *Geophy. Res. Lett*., **28**, 2361–2364.

Kraucunas, I. and D. L. Hartmann (2005), Equatorial Superrotation and the Factors Controlling the Zonal-Mean Zonal Winds in the Tropical Upper Troposphere, *J. Atmos. Sci*, **62**, 371–389.

Lebonnois, S., F. Hourdin, V. Eymet, A. Crespin, R. Fournier, and F. Forget (2010), Superrotation of Venus' atmosphere analyzed with a full general circulation model. *J. Geophys. Res.*, **115**, E06006.

Lee, C., S. R. Lewis, and P. L. Read (2005), A numerical model of the atmosphere of Venus. *Adv. Space Res.*, **36**, 2142–2145.

Lee, C., S. R. Lewis, and P. L. Read (2007), Super-rotation in a Venus general circulation model. *J. Geophys. Res*., **112**, E04S11.

Lindzen, R. S. (1990), *Dynamics in atmospheric physics*. Cambridge University Pres, 310 pp.

Lorenz, E. N. (1956), *Empirical orthogonal functions and statistical weather prediction*, Rep. 1, Statist. Forecasting Project., MIT. 52 pp.

Lorenz, E. N. (1967), *The nature of the general circulation of the atmosphere*. WMO, No. 218, TP. 115, 161 pp.

Lorenz, E. N. (1969), The nature of general circulation of the atmosphere: a present view. In: The global circulation of the atmosphere, Corby GA (ed), *Roy. Meteorol. Soc*., London, pp 2–23.

Luz, D. and F. Hourdin (2003), Latitudinal transport by barotropic waves in Titan's stratosphere: I. General properties from a horizontal shallow-water model. *Icarus*, **166**, 328–342.

Matsuno, T. (1966), Quasi-geostrophic motion in the equatorial area. *Journal of the Meteorological Society of Japan*, **44**¸ 24–43.

Mitchell, J. L. and G. K. Vallis (2010), The transition to superrotation in terrestrial atmosphere. *J. Geophys. Res*., E12008.

Mitchell, J. L., M. Ádámkovics, R. Caballero, and E. Turtle (2011), Locally enhanced precipitation organized by planetary-scale waves on Titan, *Nature Geosciences*, **4**, 589-592, doi:10.1038/ngeo1219.

Mitchell, J. L. (2012), Titan's transport-driven methane cycle. *Astrophysical Journal Letters*, **756**, L26.

Navarra, A. and G. Bocalletti (2002), Numerical general circulation experiments of sensitivity to Earth rotation rate. *Clim. Dyn*. **19**, 467–483.

Newman, C., C. Lee, Y. Lian, M. I. Richardson, and A. D. Toigo (2011), Stratospheric superrotation in the TitanWRF model. *Icarus*, **213**, 636–654.

North, G. R. (1984), Empirical Orthogonal Functions and Normal Modes. *J. Atmos. Sci.*, **41**, 879–887.

Parish, H. F., G. Schubert, C. Covey, R. L. Walterscheid, A. Grossman, and S. Lebonnois (2011), Decadal variations in a Venus general circulation model. *Icarus*, **212**, 42–65.

Pascale, S., F. Ragone, V. Lucarini, Y. Wang, and R. Boschi (2013), Nonequilibrium thermodynamics of circulation regimes in optically thin, dry atmospheres. *Planet. Space Scien.*, **84**, 48–65.

Peixoto, J. P. and A. H. Oort (1992), *Physics of Climate*. American Institute of Physics, 520 pp.

Potter, S. F., G. K. Vallis, and J. L. Mitchell (2014), Spontaneous Superrotation and the Role of Kelvin waves in an Idealized Dry GCM. *J. Atmos. Sci.*, **71**, 596–614.

Randel, W. J. and I. M. Held (1991), Phase Speed Spectra of Transient Eddy Fluxes and Critical Layer Absorption. *J. Atmos. Sci.*, **48**, 688–697.

Read, P. (2011), Dynamic and circulation regimes of terrestrial planets. *Planet. Space Scien.*, **59**, 900–914.

Richardson, M. I., A. D. Toigo, and C. E. Newman (2007), PlanetWRF: A general purpose, local to global numerical model for planetary atmospheric and climate dynamics. *J. Geophys. Res.*, **112**, E09001.

Rossow, W. B. and G. Williams (1979), Large-Scale Motion in Venus Stratosphere. *J. Atmos. Sci*, **36**, 377–389.

Saravanan, R. (1993), Equatorial Superrotation and Maintenance of the General Circulation in Two-Level Models. *J. Atmos. Sci*, **50**, 1211–1227.

Schneider, T. (2006), The general circulation of the atmosphere. *Annu. Rev. Earth Planet. Sci.* **34**, 655–688.

Shell, K. M. and I. M. Held (2004), Abrupt Transition to Strong Superrotation in an Axisymmetric Model of the Upper Troposphere. *J. Atmos. Sci.*, **61**, 2928–2935.

Skamarock, W. C., J. B. Klemp, J. Dudhia, D. O. Gill, D. M. Barker, X. Y. Huang, W. Wang , and J. G. Powers (2008), *A description of the Advanced Research WRF Version 3*, NCAR Tech. Note 475+STR, Natl. Cent. for Atmos. Res., Boulder, Colo. 125 pp.

Toigo, A., C. Lee, C. E. Newman, and M. I. Richardson (2012), The impact of resolution on the dynamics of the martian global atmosphere: Varying resolution studies with the MarsWRF GCM. *Icarus*, **221**, 276–288.

Tokano, T., F. M. Neubauer, M. Laube, and C. P. McKay (1999), Seasonal variation of Titan's atmospheric structure simulated by a general circulation model. *Planet. Space Sci*. **47**, 493–520.

Tokano, T. (2007), Near-surface winds at the Huygens site on Titan: interpretation by means of a general circulation model. *Planet. Space Sci*. **55**, 1990–2009.

Vallis, G. K. (2006), *Atmospheric and Ocean Fluid Dynamics*. Cambridge University Press. 745 pp.

Walker, C. C. and T. Schneider (2006), Eddy Influences on Hadley Circulation: Simulations with an Idealized GCM. *J. Atmos. Sci*, **63**, 3333–3350.

Wheeler, M. and G. N. Kiladis (1999), Convectively coupled equatorial waves: Analysis of clouds and temperature in the wavenumber-frequency domain. *J. Atmos. Sci.*, **56**, 374–399.

Widermann, T., E. Lellouch, and J-F. Donati (2008), Venus Doppler winds at cloud tops observed with ESPaDOns at CFHT. *Planet. Space Sci.*, **56**, 1320–1334.

Williams, G. P. (1988a), The dynamical range of global circulations — I. *Clim. Dyn*., **2**, 205–260.

Williams, G. P. (1988b), The dynamical range of global circulations — II. *Clim. Dyn*., **3**, 45–84.

Williams, G. P. (2003), Barotropic Instability and Equatorial Superrotation. *J. Atmos. Sci*, **60**, 2136–2152.

Williams, G.P. and J. L. Holloway (1982), The range and unity of planetary circulations. *Nature*, **297**, 295–299.

Yamamoto, M. and M. Takahashi (2003), The fully developed superrotation simulated by a general circulation model of a Venus-like atmosphere. *J. Atmos. Sci*., **60**, 561–574.

Yamamoto, M. and M. Takahashi (2006), Superrotation Maintained by Meridional Circulation and Waves in a Venus-like GCM. *J. Atmos. Sci*., **63**, 3296–3314.

HIGHLIGHTS:

-- Different simulations with the same nondimensional numbers have similar behavior.

-- Slowly rotating terrestrial GCM superrotates only if the thermal inertia is increased

-- Strong Hadley circulation can prevent eddies from developing superrotation.

-- Spontaneous superrotation is driven by different wave modes combination

-- Mixed baroclinic-barotropic instability may trigger the wave modes.